Kepler-68: Three Planets, One With a Density Between That of Earth and Ice Giants

Share Your Story

The Harvard community has made this article openly available.
Please share how this access benefits you. Submit a story.

Accessibility

KEPLER-68: THREE PLANETS, ONE WITH A DENSITY BETWEEN THAT OF EARTH AND ICE GIANTS

Ronald L. Gilliland[1], Geoffrey W. Marcy[2], Jason F. Rowe[3], Leslie Rogers[4], Guillermo Torres[5],
Francois Fressin[5], Eric D. Lopez[6], Lars A. Buchhave[7], Jørgen Christensen-Dalsgaard[8,9], Jean-Michel Désert[4],
Howard Isaacson[2], Jon M. Jenkins[10], Jack J. Lissauer[3], William J. Chaplin[11], Sarbani Basu[12],
Travis S. Metcalfe[13], Yvonne Elsworth[11], Rasmus Handberg[8], Saskia Hekker[14], Daniel Huber[3],
Christoffer Karoff[8], Hans Kjeldsen[8], Mikkel N. Lund[8], Mia Lundkvist[8], Andrea Miglio[11],
David Charbonneau[5], Eric B. Ford[15], Jonathan J. Fortney[6], Michael R. Haas[3], Andrew W. Howard[16],
Steve B. Howell[3], Darin Ragozzine[15], Susan E. Thompson[10],

ABSTRACT

NASA's *Kepler Mission* has revealed two transiting planets orbiting Kepler-68. Follow-up Doppler measurements have established the mass of the innermost planet and revealed a third jovian-mass planet orbiting beyond the two transiting planets. Kepler-68b, in a 5.4 day orbit, has $M_{\rm P} = 8.3^{+2.2}_{-2.4}$ $M_{\oplus}$, $R_{\rm P} = 2.31^{+0.06}_{-0.09}$ $R_{\oplus}$, and $\rho_{\rm P} = 3.32^{+0.86}_{-0.98}$ g cm^{-3}, giving Kepler-68b a density intermediate between that of the ice giants and Earth. Kepler-68c is Earth-sized with a radius, $R_{\rm P} = 0.953^{+0.037}_{-0.042}$ $R_{\oplus}$ and transits on a 9.6 day orbit; validation of Kepler-68c posed unique challenges. Kepler-68d has an orbital period of 580 ± 15 days and minimum mass of $M_{\rm P} \sin i = 0.947 \pm 0.035 M_J$. Power spectra of the *Kepler* photometry at 1-minute cadence exhibit a rich and strong set of asteroseismic pulsation modes enabling detailed analysis of the stellar interior. Spectroscopy of the star coupled with asteroseismic modeling of the multiple pulsation modes yield precise measurements of stellar properties, notably $T_{\rm eff} = 5793 \pm 74$ K, $M_{\star} = 1.079 \pm 0.051$ $M_{\odot}$, $R_{\star} = 1.243 \pm 0.019$ $R_{\odot}$, and $\rho_{\star} = 0.7903 \pm 0.0054$ g cm^{-3}, all measured with fractional uncertainties of only a few percent. Models of Kepler-68b suggest it is likely composed of rock and water, or has a H and He envelope to yield its density $\sim$3 g cm^{-3}.

Subject headings: planetary systems — stars: fundamental parameters — stars: individual (Kepler-68, KIC 11295426, 2MASS J19240775+4902249)

1. INTRODUCTION

The NASA *Kepler Mission* has presented a catalog of over 2300 stars with planet-like transit signatures (Borucki et al. 2011; Batalha et al. 2012). Here we report a detailed study of Kepler-68, a G-type main sequence star harboring a transiting planet, Kepler-68b having a radius of $\sim$2.5 $R_{\oplus}$ and orbital period, $\sim$5.40 d. We de-

scribe the detection of a second transiting planet that is close in size to the Earth. We carry out multiple follow-up measurements of the star Kepler-68 (KIC 11295426), including additional *Kepler* photometry, ground-based spectroscopy and high resolution imaging, *Spitzer Space Telescope* photometry, and Doppler measurements. At Kepler magnitude, $Kp = 10.00$, the star has high enough flux for asteroseismic analysis of its stellar properties using short cadence (see Gilliland et al. (2010)) *Kepler* photometry, offering correspondingly accurate measures of the stellar density, mass, and radius.

The photometry of Kepler-68 and subsequent transit detections of Kepler-68b and Kepler-68c are described in Section 2. We present tests performed on the *Kepler* photometry and images to rule out false positives in Section 3. We present the follow-up observations, including spectroscopy, high resolution imaging, *Spitzer Space Telescope* photometry, and precision Doppler measurements, leading to the support of Kepler-68b and Kepler-68c as planets in Section 4. We refer to the two transiting planets as Kepler-68b and Kepler-68c and the subsequent Doppler-detected outer planet as Kepler-68d. We report a corresponding Doppler signal for Kepler-68b, but the radial velocity (RV) measurements provide only an upper limit to the mass of Kepler-68c, that is physically uninteresting. We describe investigation of false-positive scenarios with a BLENDER analysis (Torres et al. 2011) as described in Section 5.

The spectroscopy and asteroseismology yield stellar

[1] Department of Astronomy, and Center for Exoplanets and Habitable Worlds, The Pennsylvania State University, 525 Davey Lab, University Park, PA 16802; gillil@stsci.edu
[2] University of California, Berkeley, CA 94720
[3] NASA Ames Research Center, Moffett Field, CA 94035
[4] California Institute of Technology, Pasadena, CA 91125
[5] Harvard-Smithsonian Center for Astrophysics, 60 Garden Street, Cambridge, MA 02138
[6] University of California, Santa Cruz, CA 95064
[7] Niels Bohr Institute, Copenhagen University, Denmark
[8] Stellar Astrophysics Centre, Dept. of Physics and Astronomy DK-8000 Aarhus C, Denmark
[9] High Altitude Observatory, National Center for Atmospheric Research, Boulder, CO 80307
[10] SETI Institute/NASA Ames Research Center, Moffett Field, CA 94035
[11] School of Physics and Astronomy, University of Birmingham, Edgbaston, Birmingham B15 2TT, UK
[12] Yale University, 260 Whitney Ave., New Haven, CT 06511
[13] White Dwarf Research Corporation, Boulder, CO 80301
[14] Astronomical Institute Anton Pannekoek, University of Amsterdam, 1098 XH Amsterdam, Science Park 904, The Netherlands
[15] University of Florida, Gainesville, FL 32611
[16] Institute for Astronomy, University of Hawaii, 2680 Woodlawn Drive, Honolulu, HI 96822

properties discussed in Section 6. The stellar density, mass, and radius permit a detailed analysis of the light curve and Doppler measurements, to give planet parameters, described in Section 7. We also discuss the properties of Kepler-68b from the standpoint of theoretical models in Section 7, especially regarding the planet's composition. Its placement in a mass-radius diagram suggests a composition of large amounts of rock and significant amounts of volatiles to yield the observed density of 3 g cm^{-3}.

With the changing status of stars during the course of the *Kepler Mission*, as planet candidates are discovered and confirmed as planets, the nomenclature used and recognized by diverse analysis groups evolves. The star studied here is located at $\alpha = 19^\mathrm{h}24^\mathrm{m}07^\mathrm{s}.75$, $\delta = +49°02'25''.0$ and in the Kepler Input Catalog (KIC) was designated KIC 11295426. The previously existing 2MASS ID was J19240775+4902249. The Kepler Object of Interest (KOI) name was given when it appeared in the Borucki et al. (2011) exoplanet candidate list as KOI00246, or the more commonly appearing KOI-246 as used herein. KOI numbers were assigned per convention as: KOI-246.01 with initial detection of the 5.4 day candidate transits, KOI-246.20 for the candidate detected based on non-*Kepler* input, and then KOI-246.02 for the second transiting planet candidate at 9.6 days. With validation and confirmation of planets the star was given its final moniker, Kepler-68, and the planets Kepler-68b,c,d – from KOIs 246.01, 246.02 and 246.20 respectively.

2. *Kepler* PHOTOMETRY

The *Kepler* instrument is described in Van Cleve & Caldwell (2009) and Argabright et al. (2008) while an overview of performance is presented in Caldwell et al. (2010b) and Jenkins et al. (2010b). Here we report the results from using 12 quarters of Kepler data. The standard pipeline reduction of the photometry first yielded a transit signal with a period of 5.40 d, consistent with a planet with a size of approximately 2.5 $R_\oplus$ (Borucki et al. 2011; Batalha et al. 2012). Subsequent searches of the light curve alerted the *Kepler* team to a second transit signal with a period of ∼9.61 d and approximately Earth size. Thus, the *Kepler* photometry and pipeline reduction from Kepler-68 reveals two periodic transit signals consistent with planets, hereafter called Kepler-68b and Kepler-68c.

Independent transit searches of the *Kepler* photometry have been carried out by Ofir & Dreizler (2012) and Huang, Bakos & Hartman (2013) who also find evidence for Kepler-68b and Kepler-68c with the same period and transit depth within uncertainties. For Kepler-68c Ofir & Dreizler (2012) find a period of 9.60538 ± 0.00026 d and a planet radius of 0.86 $R_\oplus$. They also find a single transit from a possible third planet with a transit duration of ∼8 hr implying a period of 970 ± 50 days, and planet size about 2.4 $R_\oplus$. Thus there is a possibility that a third planet transits Kepler-68. *Kepler* observations of Kepler-68 are ongoing, including acquisition of short cadence data. Inspection of data through Q13 has not shown further evidence for the several hundred day planet candidate. At a period of nearly 1000 days the next transit would not be expected until Q16 in early 2013.

Raw flux light curves for each quarter (Jenkins et al.

2010a) are corrected for systematic errors, detrended, and stitched together to form contiguous time series, and are then searched for transit signals (Jenkins et al. 2010d). We remove systematic errors, outliers and intra-quarter discontinuities by co-trending against the photometry of other stars in the vicinity of Kepler-68 using the Pre-Search Data Conditioning (PDC) pipeline module as described in Twicken et al. (2010b), with updates as per Stumpe et al. (2012); Smith et al. (2012).

Figure 1 shows the raw (SAP_FLUX, the result of simple aperture photometry) and corrected (PDC-SAP_FLUX) flux time series for Kepler-68 during a representative quarter (Q4). The largest remaining systematic errors in the PDC-MAP (Stumpe et al. (2012); Smith et al. (2012)) processed data are minor offsets following thermal transients after monthly pointing changes to telemeter data to the ground (very small for Q4). The slow variation with a period of ∼50 days and amplitude of 0.0003 in this figure could either be intrinsic to the star, or associated with imperfect removal of long-term drifts due to image motion (differential velocity aberration) that is present in the raw data. It is clear that variations in Kepler-68 are smaller than typical variations of the Sun, consistent with the slow rotation and advanced age argued for in sections 6.1 and 6.2 respectively. After filtering out transit events, the measured relative standard deviation of the PDC-corrected, long-cadence light curve is 21 ppm per 6 hour interval (CDPP – the formal Combined Differential Photometric Precision – see Jenkins et al. (2010b), and Christiansen et al. (2012b)). An expected instrument + photon noise is computed for each flux in the timeseries. The mean of the per (29.4-minute) cadence noise estimates reported by the pipeline is 233 ppm. Both raw (simple aperture sums) and corrected (PDC-MAP) light curves are available at the Mikulski Archive for Space Telescopes (MAST)[17] at the Space Telescope Science Institute.

2.1. *Transiting Planet Search*

The Kepler-68b transits were identified by the Transiting Planet Search (TPS) pipeline module that identifies periodic reductions in flux having a duration of hours, each corresponding to a transit of a prospective planet. The algorithm is a wavelet-based, adaptive matched filter (Jenkins et al. 2010d). TPS then identifies a time series of single "events", each having an associated "single event statistic (SES)" that represents the probability that a transit is present. The SES from each transit are combined into multiple event statistics (MES) by folding them at trial orbital periods ranging from 0.5 days to as long as half the data coverage interval.

Kepler-68b was identified by TPS in each quarter of data with a multiple event statistic $> 15\sigma$.

Multi-quarter searching for transits was used. The transit depth, duration, period, and epoch are derived from physical modeling (see Section 7) using all of the available data. Kepler-68b is characterized as a 345.6 ± 1.5 ppm dimming lasting 3.459 ± 0.009 hours with transit ephemeris of T [BJD] $= 2455006.85729 \pm 0.00042 + N * 5.398763 \pm 0.000004$ days. The longer-period transits of Kepler-68c were identified by non-pipeline inspections. Kepler-68c is characterized as a 53.1 ± 2.3 ppm dimming

[17] http://archive.stsci.edu/kepler

lasting 3.09 ± 0.09 hours and an ephemeris $\mathrm{T\,[BJD]} = 2454969.3805 \pm 0.0041 + N*9.605085 \pm 0.000072$ days.

3. DATA VALIDATION

Signals that mimic planet transits are also found by TPS. All "threshold crossing events" identified by TPS are subjected to assessment of standard vetting products that allow separate disposition of clear false positives before bestowing the KOI moniker. Most false positives can be identified by judicious assessment of the quality of the transit-planet model fit to the photometry and by searching for astrometric displacements of the photo-center between times out of transit and in-transit. True transiting planets should exhibit photometry that is well fit by a transiting planet model and they should show little, if any, astrometric displacement during transit (depending on neighboring stars). Such "Data Validation" techniques are described in Batalha et al. (2010) and in Batalha et al. (2011). Both Kepler-68b and Kepler-68c passed all such tests, conferring KOI planet candidate status for both of them, as will be further discussed next.

Figure 2 shows several representations of data relevant to judging the Kepler-68b signal. In some early quarters the optimal aperture did not encompass all of the flux, especially for saturated targets like Kepler-68. This leads to suppressed variation and is the reason we did not use the Q3 data. The upper panel shows the phase folded light curve for Kepler-68b, after de-trending and subtraction of the Kepler-68c transit signal. A common type of false positive is a background eclipsing binary blended with the target star; in such cases a secondary eclipse is often seen. No evidence of a secondary eclipse is seen here, nor turned up in automated searches. The lower left panel shows that the phase folded data for Kepler-68b are fit very well by our transit model. Another signature of a possible false positive associated with an eclipsing binary (either the target star itself as a grazing eclipse or as a blended background system) relies on searching for subtle differences of depth between alternate transits – a binary with twice the listed period and primary and secondary eclipses of slightly unequal depths are easily seen in data of this quality. From all aspects of lightcurve inspection Kepler-68b is entirely clean.

Figure 3 addresses Kepler-68c showing analogous vetting products for the time series as Figure 2, but with the transit signal of Kepler-68b subtracted out. Again, there is no clear evidence for a secondary eclipse, or depth differences for alternately averaged transits, either of which would be suggestive of a false positive interpretation. The question of a secondary eclipse feature will, however, be explored at depth in the BLENDER context in Section 5. This transit, that is only ∼60% as deep as a true Earth analog, obviously appears at high signal-to-noise in the phase folded data and is well fit by our planet transit model.

Centroid analyses based on assessing the in- and out-of-transit signal positions can be particularly powerful, (e.g. see Batalha et al. (2011) for application to Kepler-10b). The difference of average images taken out-of-transit, minus a similar average of images taken during transit for an unsaturated target yields a PSF at the inherent source position (coincident within errors with the target star for a clean candidate). Since Kepler-68 is saturated, the centroid analyses are much less discerning

with the inherent loss of spatial information following saturation. For a strongly saturated target changes of flux are concentrated at the end of bleed columns, while the central pixels in the bleed trail remain, well, saturated.

The KIC shows the location of a fainter (magnitude not available in KIC, but derived below in Section 4.2.1 from AO imaging) star offset by about $11''$ in such a way that it is almost precisely in the detector column direction from Kepler-68. In most quarters Kepler-68 is roughly centered on a pixel in the column direction leading to bleeding that encompasses this secondary star, KIC 11295432, in which circumstance using the Kepler data to discern the true source of transits between the two stars is not possible. In Q9 both Kepler-68 and the fainter neighbor KIC 11295432 are nearly centered between columns, and the bleeding terminates before reaching the latter. Table 1 details pixel values in both the direct out-of-transit image at the left, and for the difference images of Kepler-68b and Kepler-68c in the central and right blocks for Q9 data. (Q1 and Q5 with the telescope at the same orientation also possess this feature, but the Kepler-68c difference images, which in the best of circumstance are low signal-to-noise, were unstable for these quarters.) The difference images for both Kepler-68b and Kepler-68c show maxima in the terminal saturation pixels, rather than in the pixel containing KIC 11295432. This proves that KIC 11295432 cannot be the source for either set of transits. Saturated pixels in these quarters span a rectangle of 2×4 pixels, or $8'' \times 16''$ for which centroid analysis does not rule out background contaminating sources. Deviations in the difference image along the row direction for saturated images likely result from imperfect correction for LDE (local detector electronics) undershoot (Caldwell et al. 2010a), a signal-dependent offset to negative values along rows traced to an amplifier in the Kepler electronics. The high resolution imaging discussed in Section 4.2 will provide the primary constraints on potential background objects, which if these objects were eclipsing binaries could be the source of false positives.

In Figure 4 we present vetting evidence to further investigate the veracity of the single transit of presumed long period reported in Ofir & Dreizler (2012) and shown in their Fig. 3. The detrending of raw Kepler data adopted by Ofir & Dreizler (2012) results in a ∼8 hour wide intensity drop that is adequately fit with a standard transit model. In the raw LC (simple aperture photometry – no detrending) Kepler data their event is easily seen at BJD - 2455000 = 403.2. However, the raw LC data shows a drop of intensity across this event of about 0.0001 which may be easily seen by drawing linear fits to the data before or after the event. Such behavior is commonly seen with sudden pixel sensitivity losses associated with radiation damage to a single pixel (see, e.g. discussion from discovery in HST ACS data by Gilliland & Bohlin (2007) and Christiansen et al. (2012a) for presence in Kepler data) – and ultimate recovery of most, but not all of the depressed sensitivity. Such sensitivity drops can be particularly difficult to tell from transits in LC data which blur both sudden (spurious) drops, and short ingress/egress events. The spurious signature may be more easily seen in short cadence data as shown in the bottom panel of Figure 4 – here the event looks more

like a sudden sensitivity loss and recovery, than a transit. Note that the two occurrences of Kepler-68b transits about one day from both ends show symmetric responses about the transit centers, while the single-event behavior is quite asymmetric with shape characteristic of a pixel sensitivity loss. The middle panel shows that the pipeline PDC-MAP treatment completely removes any suggestion of the single-event transit while nicely preserving the real events from Kepler-68b. These considerations do not prove the single-event transit as an instrument systematic false positive, but this interpretation is favored by us. Definitive proof would come if a difference image analysis across transit could isolate the intensity drop to one pixel, while the stellar signal spans several pixels. We tested for this, but were only able to show that the source is within the set of saturated pixels for Kepler-68, leaving open an astrophysical source.

4. FOLLOW-UP OBSERVATIONS

Kepler-68 was identified as having a candidate planet in late 2009, prompting follow-up observations to confirm and characterize the planet, and to secure more precise stellar parameters than are available in the Kepler Input Catalog. We were particularly interested in checking for signs of a nearby eclipsing binary star system that might masquerade as a planet. We carried out spectroscopy of the host star Kepler-68 (Section 4.1) and high spatial resolution imaging to identify nearby stars in the photometric aperture (Section 4.2). Upon passing those gates, we carried out high-resolution, high signal-to-noise ratio (SNR) echelle spectroscopy with and without an iodine cell to measure atmospheric stellar parameters, magnetic activity, absorption line shape changes with time, and to make precise Doppler measurements. As described below, these follow-up observations revealed no evidence of a nearby eclipsing binary for either transiting planet, and they provide measurements and constraints on the masses of the transiting planets. In addition, a previously unknown non-transiting planet was revealed as discussed in Section 4.3. Bisector analyses of the high resolution spectroscopy are presented in Section 4.4. We obtained *Spitzer Space Telescope* photometry through transits of Kepler-68b and present results in Section 4.5.

4.1. *Reconnaissance Spectroscopy*

Two reconnaissance spectra were obtained with the Tull Coude Spectrograph of the McDonald Observatory 2.7m Harlan J. Smith Telescope on the nights of 25 March 2010 and 28 March 2010, and a third at the TRES Echelle Spectrograph of the Tillinghast 1.5m telescope on Mt. Hopkins, also on the night of 25 March 2010. These high spectral resolution, low signal/noise spectra showed no convincing evidence for radial velocity variability at the $0.2 \, \mathrm{km \, s^{-1}}$ level, and no hints of any contaminating spectra. These spectra were cross-correlated against a library of synthetic model stellar spectra as described by Batalha et al. (2011) in order to derive basic stellar parameters to compare with the Kepler Input Catalog (KIC) values. These spectra were in excellent agreement, and yielded $T_{\mathrm{eff}} = 5750\mathrm{K}$, $\log g = 4.0$, and rotational velocity less than $4 \, \mathrm{km \, s^{-1}}$. The height of the cross-correlation peaks ranged from 0.93 to 0.96, indicating an excellent match with the library spectra. This spectroscopy suggests that Kepler-68 is a sun-like, slowly

rotating main sequence star, in support of the planetary interpretation for the transit events.

4.2. *High Resolution Imaging*

There is always a possibility, especially for bright stars of high enough proper motion for old plates to reveal the background distribution of faint stars in the current epoch. Inspection of 1953 and 1991 Sky Survey plates shows that this does not work for Kepler-68 – the proper motion is far too small.

4.2.1. *AO Imaging*

Near-infrared adaptive optics imaging of Kepler-68 was obtained with the 6.5 m MMT telescope on Mt. Hopkins and the Arizona Infrared imager and Echelle Spectrograph (ARIES). The Kepler-68 imaging was obtained on the night of 2010 May 5 (UT) using the f/30 mode with a field of view of $20'' \times 20''$ and a resolution of $0\farcs02085$ per pixel. The AO system guided on the primary target. The FWHM of the J band combined image was $0\farcs123$, while the Ks band provided $0\farcs112$ imaging. A four-point dither pattern was used with a total of 16 images in each band. Further details of the MMT-ARIES high resolution imaging for *Kepler* follow-up support may be found in Adams et al. (2012).

Figure 5 shows a region of the ARIES Ks band image. Within the domain plotted no other sources are visible to the 5-σ depth limits as shown in Figure 6. Within the full ARIES field of view one additional source at 6.1 and 5.7 magnitudes fainter in J and Ks respectively was identified. Using the 2MASS J and Ks magnitudes for Kepler-68 of 8.974 and 8.587 leads to estimates of 15.07 and 14.29 respectively for the companion. Using the transformations in Appendix A of Howell et al. (2011) leads to a $Kp = 17.0 \pm 0.4$, or a δ-magnitude of 7.0 ± 0.4 with respect to Kepler-68 in the *Kepler* bandpass. This AO identified source also shows up clearly in available UKIRT J direct imaging (Lucas & Samuel 2009) and corresponds to the star KIC 11295432, which does not have a specified Kp in the KIC. From a combination of *Kepler* data centroid consideration (Section 3), and the ARIES AO, and UKIRT data, to roughly the exclusion limits reached in Figure 6, no other sources exist to relevant larger radii as well.

4.2.2. *Speckle Imaging*

Speckle imaging of Kepler-68 was obtained on the night of 2010 June 20 UT using the two-color speckle camera at the Wisconsin Indiana Yale NOAO (WIYN) 3.5-m telescope on Kitt Peak. The speckle camera simultaneously obtained 1000 40 msec images in two filters: V (5620/400Å) and R (6920/400Å). These data were reduced and processed to produce a final reconstructed speckle image for each filter. Figure 5 includes this speckle-reconstructed R band image. The details of the two-color speckle camera are presented in Howell et al. (2011) for application in the *Kepler* follow-up program.

The speckle data allow detection of a companion star within the approximately 2.76 × 2.76 arcsec box centered on the target. The speckle imaging can detect, or rule out, companions between 0.05 arcsec and 1.5 arcsec from Kepler-68. We found no companion star within the speckle image to the detection limits shown in Figure 6.

When high quality near-IR AO imaging is available, as in this case, the WIYN speckle imaging is largely redundant providing unique sensitivity for a small angular separation range due to its superior FWHM of $0\rlap{.}''053$ – a factor of two sharper, but generally shallower than the MMT AO imaging.

4.3. *Precise Doppler Measurements of Kepler-68*

We obtained 52 high resolution spectra of Kepler-68 between 2010 July 19 and 2012 Aug 12 using the HIRES spectrometer on the Keck I 10-m telescope (Vogt et al. 1994). We configured the spectrometer, took observations, and reduced the spectra with the same method used on thousands of nearby FGKM stars (Marcy et al. 2008). This technique yields a Doppler precision of 1.0-1.5 $\mathrm{m\,s^{-1}}$ for stars as faint as 14th magnitude (V band), depending on spectral type and rotational $v \sin i$. The HIRES fiber-feed was not used for these observations. An iodine cell was used to superimpose iodine lines on the stellar spectrum, providing empirical information for each exposure and each wavelength about the instantaneous wavelength scale and instrumental profile of the spectrometer.

The observations were made with the "C2 decker" entrance aperture which projects to $0\rlap{.}''87 \times 14\rlap{.}''0$, giving a resolving power of about 60,000 at 5500 Å and enabling sky subtraction (typical seeing is $0\rlap{.}''6 - 1\rlap{.}''2$). The average exposure was 11 minutes, giving a signal-to-noise ratio per pixel of 200.

The raw CCD images were reduced in the standard way, including the subtraction of background sky counts (mostly from moonlight) at each wavelength just above and below the stellar spectrum. We used Doppler analysis with the algorithm of Johnson et al. (2009). The internal Doppler errors (the weighted uncertainty in the mean of 400 spectral segments) are typically 1.0-1.5 $\mathrm{m\,s^{-1}}$. Our experience with hundreds of G-type main sequence stars shows that the actual errors are larger than the internal errors by $\sim$1.5 $\mathrm{m\,s^{-1}}$ for such stars. Thus, we added 1.5 $\mathrm{m\,s^{-1}}$ in quadrature to the internal uncertainties to yield our estimated uncertainty in the RV. The resulting velocities and uncertainties are given in Table 2 and shown in Figure 7 as a function of time. The error bars include the internal Doppler errors and an assumed jitter of 1.5 $\mathrm{m\,s^{-1}}$.

The center of mass velocity relative to the solar system barycenter (Gamma Velocity) for Kepler-68 is -20.9 ± 0.1 km s^{-1} (Table 4). This is a typical radial velocity for a star in the Galactic disk, indicative of a middle-aged disk star. The near solar metallicity (Section 6.1), [Fe/H] = $+0.12 \pm 0.074$, magnetic activity (Section 6.1), and asteroseismic age, 6.3 ± 1.7 Gyr (Section 6.2), also suggest Galactic disk membership.

The primary signal from the RVs is the $K = 19.9 \pm 0.75$ m s^{-1} variation with a period of 580 ± 15 days as shown first in Figure 7, and phased in Figure 8. This clear RV signature, coupled with the lack of bisector variations discussed in Section 4.4 provides discovery and confirmation of the Jovian-scale outer planet – Kepler-68d.

The velocities phased to the photometric period of Kepler-68b in Figure 8 show a clear, continuous, and nearly sinusoidal variation consistent with a nearly circular orbit of a planetary companion. Note that the 7 magnitude (see Sections 3 and 4.2.1) fainter companion KIC 11295432 blended into the *Kepler* photometry does not fall within the HIRES slit and cannot be the source of Kepler-68b radial velocity variations. The lack of any discontinuities in the phased velocity plot argues against a background eclipsing binary star as the explanation. Such a binary with a period of 5.4 d would have orbital semi-amplitudes of tens of kilometers per second, so large that the spectral lines would completely separate from each other, and separate from the lines of the main star. Such breaks in the spectral-line blends would cause discontinuities in the velocity variation, which are not seen here. Thus, the chance that the 5.4 d periodicity exhibited independently in both the photometry and velocities might be caused by an eclipsing binary seems small.

Precision Doppler measurements are used to constrain the mass of Kepler-68b as discussed in Section 7. The absence of a Doppler signal for Kepler-68c is used to compute an upper limit to the mass under the planet interpretation.

4.4. *Bisector Analysis*

From the Keck spectra, we computed a mean line profile and the corresponding mean line bisector. Time-varying line asymmetries are tracked by measuring the bisector spans – the velocity difference between the top and bottom of the mean line bisector – for each spectrum (Torres et al. 2005). When radial velocity variations are the result of a blended spectrum between a star and an eclipsing binary, we expect the bisectors to reveal a phase-modulated line asymmetry (Queloz et al. 2001; Mandushev et al. 2005).

The bisector spans in the lower panel of Figure 7 show no correlated variation with the radial velocities and have a scatter of 7.8 $\mathrm{m\,s^{-1}}$, which is significantly less than the semi-amplitude of Kepler-68d. However, the uncertainties in the bisector measurements are larger than the semi-amplitude of the two smaller planets in the system and a bisector analysis is thus inconclusive with respect to Kepler-68b and Kepler-68c.

4.5. *Photometry with the Spitzer Space Telescope*

Kepler-68b was observed during two transits with *Warm-Spitzer*/IRAC (Werner et al. 2004; Fazio et al. 2004) at 4.5 μm (program ID 60028). The observations occurred on UT 2010 December 27 and on UT 2011 January 7. The visits lasted 7.6 hours. The data were gathered in subarray mode (32×32 pixels) with an exposure time of 2 s per image which yielded 15680 images per visit.

The images used are the Basic Calibrated Data (BCD) delivered by the *Spitzer* archive. These files are corrected for dark current, flat-fielding, detector non-linearity and converted into flux units. The method we used to produce photometric time series from the images is described in Désert et al. (2009). We first discard the first half-hour of observations, which are affected by a significant telescope jitter before stabilization. To facilitate the evaluation of the photometric errors, we then convert the pixel intensities to electrons using the information given in the detector gain and exposure time provided in the

FITS headers. We convert to UTC-based BJD following the procedure developed by Eastman et al. (2010). We correct for transient pixels in each individual image using a 20-point sliding median filter of the pixel intensity versus time. We find the centroid position of the stellar point spread function (PSF) and perform aperture photometry using a circular aperture with a radius of 3.5 pixels on individual BCD images; we adopt the radius which provides the smallest errors. The final number of photometric measurements used is 13146 data points for the first visit and 13262 for the second one. The raw time series are presented in the top panels of Figure 9. We find a typical signal-to-noise ratio (SNR) 260 per image which corresponds to about 90% of the theoretical signal-to-noise.

We used a transit light curve model multiplied by instrumental decorrelation functions to measure the transit parameters and their uncertainties from the *Spitzer* data as described in Désert et al. (2011a). We compute the transit light curves with the IDL transit routine OCCULTSMALL from Mandel & Agol (2002). In the present case, this function depends on one parameter: the planet-to-star radius ratio $R_p/R_\star$. The other transit parameters are fixed to the value derived from the *Kepler* lightcurves. The limb-darkening coefficients are set to zero consistent with expected small values in the IR and insufficient photometric precision in the *Spitzer* light curves to matter.

The *Spitzer*/IRAC photometry is known to be systematically affected by the so-called *pixel-phase effect* (see e.g., Charbonneau et al. 2005; Knutson et al. 2008). We decorrelated our signal in each channel using a linear function of time for the baseline (two parameters) and a quadratic function of the PSF position (four parameters) to correct the data for each channel. We performed an MCMC analysis with six chains of length 10^5 each providing median depth values and errors. We allow asymmetric error bars spanning 34% of the points above and below the median of the distributions to derive the 1 σ uncertainties for each parameter as described in Désert et al. (2011b).

We measured the transit depth for Kepler-68b at 4.5 μm of 350 ± 70 ppm for the first and 560 ± 70 ppm for the second visit. The weighted mean of these two values provides a transit depth of 455 ± 50 ppm. The value for the first visit is in excellent agreement with the *Kepler* depth of 346 ppm suggesting that the radius-ratio of the candidate Kepler-68b to its host star is a wavelength independent function, in agreement with a dark planetary object. However, visit two is 3 σ from the *Kepler* value. Two possibilities for this behavior, other than the small statistical probability of two such discrepant values legitimately following from the same underlying distribution, are: (1) a physically different depth in the two epochs for the transit, and (2) an inconsistency in one of the *Spitzer* epochs that we have failed to uncover. To investigate the first possibility we identified the position of the two *Spitzer* epochs relative to *Kepler* coverage. Alas, despite the excellent overall duty cycle with *Kepler* in excess of 90%, both epochs fell into the longest downtime experienced to date with *Kepler* – due to a safing event before Q8. We have no data with which to challenge the hypothesis that the two epochs really do have different depths, as could happen if there is an as yet unclaimed

transiting planet that overlapped with the deeper *Spitzer* transit of Kepler-68b. We have not uncovered direct evidence for an inconsistency in the data quality or analyses sufficient to explain the discrepancy in depths of the two *Spitzer* epochs. However, we do note that the scatter evident in Figure 9 for the anomalously deep transit is much larger than we normally encounter.

Given the perfect agreement of one *Spitzer* visit in reproducing the transit depth seen in the optical, the radial velocity confirmation documented in the previous section, and a strong BLENDER validation to be presented in Section 5 the case for the planet interpretation of Kepler-68b remains strong.

5. BLENDER ANALYSIS OF THE *Kepler* LIGHT CURVE

In this section we examine the possibility that the transit signals seen in the *Kepler* photometry of Kepler-68 are the result of contamination of the light of the target by an eclipsing object along the same line of sight. We begin with the more difficult signal Kepler-68c, which would correspond to an Earth-size planet.

5.1. *Validation of Kepler-68c*

In the absence of a dynamical confirmation of the planetary nature of the Kepler-68c signal from either a Doppler detection or a Transit Timing Variation (TTV) signature, we proceed here with a probabilistic "validation". In essence, we seek to demonstrate that the signal is much more likely to be caused by a bona-fide transiting planet than by a false positive (or "blend"). For this we applied the BLENDER procedure, which has been described previously (Torres et al. 2004; Fressin et al. 2011, 2012a) and used to validate a number of other *Kepler* planets (e.g., Ballard et al. 2011; Lissauer et al. 2012; Borucki et al. 2012; Howell et al. 2012; Gautier et al. 2012). We refer the reader to these works for full details of the method.

Briefly, we performed a systematic exploration of the different types of false positives that can mimic the signal, by generating large numbers of synthetic blend light curves over a wide range of parameters and comparing each of them with the *Kepler* photometry in a χ^2 sense. The photometry we used for the validation is the detrended short-cadence time series (one month from Q2, plus the seven quarters of Q5–Q11 – 886,638 measurements), which provides stronger constraints on the shape of the transit than the long cadence data, as shown later. We rejected blends that result in light curves inconsistent with the *Kepler* observations. We then estimated the frequency of the remaining blends by taking into account all available observational constraints from the follow-up observations mentioned above. Finally we compared this frequency with the expected frequency of true planets (planet "prior") to derive the odds ratio.

The types of false positives we considered include eclipsing systems falling within the *Kepler* aperture that are either in the background or foreground, or that are physically associated with the target in a hierarchical triple configuration. We allowed the object producing the eclipses to be either a star or a planet. To compute the blend frequencies we used informed estimates of the number density of stars in the background from the Besancon Galactic structure model of Robin et al. (2003), rates of occurrence of eclipsing binaries in the *Kepler*

field from the work of Slawson et al. (2011), and frequencies of planets involved in blends based on the catalog of planet candidates (KOIs) of Batalha et al. (2012), which was constructed using observations from Q1 to Q6. The same catalog was also used to estimate the planet prior. This list of KOIs is bound to contain some fraction of false positives (see, e.g., Morton & Johnson 2011; Morton 2012) and it is also likely incomplete mainly due to the difficulty in detecting shallow signals especially with long periods. Consequently we have applied corrections for these effects following a Monte Carlo procedure described by Fressin et al. (2012b), both in computing the blend frequencies and also for the planet prior.

The observational constraints used to further reduce the number of blends included the following: (a) the color of the star as reported in the KIC (Brown et al. 2011), which allows us to rule out any simulated blends resulting in a combined color that is significantly redder or bluer than the target; (b) limits from the centroid motion analysis on the angular separation of companions that could produce the signal (Section 3); (c) brightness and angular separation limits from high-resolution adaptive optics and speckle imaging (Section 4.2); (d) limits on the brightness of unresolved companions from high-resolution spectroscopy (Section 4.1). For eclipsing systems physically associated with the target we considered also dynamical stability constraints in hierarchical triple configurations (Holman & Wiegert 1999).

The BLENDER simulations for Kepler-68c rule out all false positive scenarios involving eclipsing binaries physically associated with the target, as the predicted light curves invariably have the wrong shape to match a planetary transit. For the scenarios involving eclipsing binaries that are in the background or foreground we find a blend frequency of 2.8×10^{-6}, and for those in which larger planets transit background stars we estimate a much smaller frequency of 7.0×10^{-8}. Hierarchical triples (a larger planet transiting a stellar companion to the target) contribute a frequency of 6.7×10^{-7}. The total blend frequency is thus 3.5×10^{-6}. An illustration of the constraints on false positives resulting from BLENDER as well as those from the follow-up observations is given in Figure 10.

An estimate of the planet prior may be obtained by dividing the number of known planets of similar size as Kepler-68c from Batalha et al. (2012) by the total number of main-sequence *Kepler* targets observed during Q1–Q6, which is 138,253. We find 71 KOIs that are in the same (3σ) radius range as the putative planet in Kepler-68c, of which we expect 9.4 to be false positives, following the procedures of Fressin et al. (2012b). We also expect such shallow ($\sim$50 ppm) transit signals to be detectable around only about 9.7% of all *Kepler* targets, which we use to correct for incompleteness. We compute the planet prior as $(71 - 9.4)/0.097/138{,}253 = 4.6 \times 10^{-3}$. This *a priori* planet frequency is $4.6 \times 10^{-3}/3.5 \times 10^{-6} \approx 1300$ times larger than the estimated blend frequency, from which we conclude that Kepler-68c is validated as a true planet with a very high degree of confidence.

In the above calculations we have not explicitly taken into consideration the period of the signal, which may be an important factor for small candidates such as Kepler-68c because such signals are relatively rare in the KOI list of Batalha et al. (2012). This may in principle influence both the planet prior and the blend frequencies we have just described, given that the latter also draw on the KOI list to estimate the rate of occurrence of larger planets involved in blends. Therefore, instead of allowing eclipsing binaries and transiting planets with any orbital period for the blend frequency calculations, we repeated the analysis with the more realistic approach of accepting only blends with periods near the measured period of Kepler-68c (within a factor of two). We did the same when computing the planet prior, for consistency. The total blend frequency is reduced in this way by about a factor of five, but the new planet prior is only 1.5 times smaller, resulting in a larger net odds ratio of $\sim$4300 that provides for an even stronger validation than before.

The above calculations neglect the fact that KOI-246.02 was found around a target that has a statistically validated transiting planet, KOI-246.01 = Kepler-68b. The planet priors used were averaged between single and multi-planet systems. Actual planet priors are about 30% smaller for single planets and more than an order of magnitude larger for multiple planets (Lissauer et al. 2012, 2013). The presence of a known planet also increases the prior for physically-associated blends, but by a smaller factor. The numbers quoted above for the likelihood of false positives are four times higher for background blends than for physically-associated blends, so when multiplicity of the system is accounted for, the odds ratios against blends quoted above are increased by roughly an order of magnitude.

As an interesting test of the value of short cadence versus long cadence data for false positive discrimination, we repeated the calculations with the long-cadence time series (Q1–Q2, Q4–Q11, 34,556 measurements) including the period cut described above. We find an odds ratio of approximately 1500, about three times lower than when using short cadence, but still large enough to comfortably validate the signal. Therefore, at least for Kepler-68c, short cadence provides a clear advantage in ruling out blends. This is likely due to the better definition of the transit shape at ingress/egress, which is often where the main differences are between model light curves for blends and the model for a true planet. In this case we find that the main improvement (decrease) in the blend frequencies when going from long to short cadence is in the scenarios involving hierarchical triples, with background eclipsing binary frequencies changing the least.

While in principle the above calculations provide a clear statistical validation of the Kepler-68c signal as a true planet, independently of the detection of the reflex motion of the star (radial velocities), we note that some of the blend scenarios involving background eclipsing binaries yield a fit to the *Kepler* photometry that is significantly *better* than that of a planet fit. This is a situation we have not encountered in previous validations of *Kepler* candidates. The light curves of these false positive scenarios all feature a very shallow ($\sim$10 ppm) secondary eclipse that happens to match a similar dip present in the phase-folded photometry for Kepler-68c at phase 0.5. This shallow dip at phase 0.5 has a formal significance of $3 - 4 \sigma$, and is the primary source for these favorable false positive fits.

The reality of the signal at phase 0.5 for Kepler-68c is in doubt; were this not so claiming validation in this case

would be impossible. Figure 11 contrasts phase folded short cadence data for Kepler-68c at both the transit, and offset by half phases. In assessing the reality of this putative secondary eclipse feature we have examined the data in several ways. When averaged over widths comparable to the transit the data show a few other excursions (both positive and negative) to deviations as large as the phase 0.5 feature; thus the feature is obviously not highly significant. However, other aspects of data investigation do not support a straightforward dismissal of evidence consistent with the weak, ~10 ppm feature. Examination of medians over the phase bins shown in Figure 11 showed the same offsets, thus the deviation does not result simply from a small subset of the data. Likewise, dividing the data into first and second halves before doing independent phase binnings shows evidence for a ~10 ppm depression at phase 0.5 in both cases. In these two halves there are again other instances of deviations of comparable width and depth; however, across the two halves the only cases lining up are those at phase 0.5. While nothing here is convincing in terms of regarding the phase 0.5 offset as real, it is equally the case that the reality of the offset cannot be excluded. We therefore took the conservative approach of allowing BLENDER to be influenced by the apparent negative offset at phase 0.5, which still provides the favorable odds ratio required for formal validation of Kepler-68c as a planet.

Further complicating this interpretation these data show a small degree of correlated noise, even after folding over 64 orbits of Kepler-68c. After binning to 0.001 phase bins the first autocorrelation value is 0.25, falling to zero within about 0.005 in phase. We formed simulated time series consisting only of Gaussian noise, stellar oscillations, and granulation (Gilliland et al. 2011b) appropriate to Kepler-68 and found that after folding this had a similar (although smaller) degree of autocorrelation suggesting that inherent stellar variations may suffice to explain the modest correlated noise.

5.2. *Validation of Kepler-68b*

The robust detection of a Doppler signal at the period of Kepler-68b provides strong support for the planetary nature of that signal. There is, however, a small chance that a background eclipsing binary could mimic this spectroscopic signature of a planet (as well as the photometric signal), although this possibility was convincingly argued against in Section 4.3. The precision of our bisector span measurements in Section 4.4 is not quite high enough for a definite conclusion regarding this possibility, so we proceed here with a validation analysis along the lines of what was done for Kepler-68c.

The much deeper transit (~350 ppm) and higher signal-to-noise ratio of Kepler-68b result in significantly stronger constraints on the shape of the signal, and consequently in a much reduced frequency of blends that give acceptable fits to the *Kepler* light curve. Indeed, background eclipsing binaries are completely ruled out by BLENDER, as no such scenarios yield light curves with a transit shape that matches the observations sufficiently well. And while some hierarchical triple scenarios are allowed by BLENDER, the companion stars would all be bright enough that they would have been seen in our high-resolution spectra. The only remaining blend scenarios that are viable are those involving larger planets

transiting a background or foreground star. We estimate the frequency of such blends to be 1.4×10^{-8}.

To estimate the a priori likelihood of a true planet we use the fact that there are 96 candidates in the list of Batalha et al. (2012) with a similar planetary radius as that implied by Kepler-68b (within 3σ), of which an estimated 6 should be false positives. Signals of this kind are expected to be detectable in 58.7% of all *Kepler* targets. The planet prior is then $(96 - 6)/0.587/138{,}253 = 1.1 \times 10^{-3}$. With this we obtain an odds ratio of nearly 79,000 in favor of the planet interpretation, i.e., a very clear validation of Kepler-68b. The above results used the long-cadence time series for simplicity, and included the period cut described above. Use of short cadence would likely result in an even higher odds ratio. For completeness we note that Morton & Johnson (2011) reported a false positive probability of 0.01 for Kepler-68b, whereas our confidence level is orders of magnitude better. Their result was based on a less sophisticated analysis, much less *Kepler* data, and didn't make use of any of the follow-up observations that we have utilized.

6. STELLAR CHARACTERISTICS

6.1. *Spectroscopic Parameters*

We did a spectral synthesis analysis using SME (Valenti & Piskunov 1996; Valenti & Fischer 2005) of one of our high resolution template spectra from Keck-HIRES of Kepler-68 to derive an effective temperature, $T_{\rm eff} = 5754 \pm 44$ K, surface gravity, $\log g = 4.2 \pm 0.1$ (cgs), metallicity, $[{\rm Fe/H}] = +0.10 \pm 0.04$, and $v \sin i = 0.5 \pm 0.5$ km s^{-1}.

The above effective temperature was used to constrain the fundamental stellar parameters derived via asteroseismic analysis (see Section 6.2). The asteroseismology analysis gave $\log g = 4.281 \pm 0.008$ which is 0.1 dex higher than the SME value. The asteroseismology value is likely superior because of the high sensitivity of the acoustic periods to stellar radius. Still, the asteroseismology result depended on adopting the value of $T_{\rm eff}$ from SME. We recomputed the SME analysis by freezing (adopting) the seismology value for $\log g$. See Torres et al. (2012) for a recent discussion of such iteration in the analogous context of high SNR transit light-curve analysis providing the $\log g$ "truth". This iteration yielded values of $T_{\rm eff} = 5793 \pm 44$ K, $[{\rm Fe/H}] = +0.12 \pm 0.04$, and rotational $v \sin i = 0.5 \pm 0.5$ km s^{-1}. The revised effective temperature was then put back into the asteroseismology calculation to further constrain the stellar radius and gravity. This iterative process converged quickly, as the $\log g$ from seismology yielded an SME value for $T_{\rm eff}$ that was only slightly different from the original unconstrained determination, and the asteroseismic $\log g$ using the iterated $T_{\rm eff}$ remained at 4.281. Likely systematic errors on $T_{\rm eff}$ and $[{\rm Fe/H}]$ of 59 K and 0.062 dex have been derived by Torres et al. (2012) in comparing results across multiple spectroscopic packages for a large number of stars. Adding these additional errors in quadrature with the errors quoted above results in more resonable total errors of 74 K and 0.074 dex.

We measured the Ca II H&K emission (Isaacson & Fischer 2010), yielding a Mt. Wilson S value, $S=0.139$ and $\log R'_{\rm HK} = $-5.15. These values suggest lower activity for Kepler-68 in comparison to mean solar reported as $S = $

0.178, $\log R'_{\mathrm{HK}}$ = -4.90 by Lockwood et al. (2007) and S = 0.171, $\log R'_{\mathrm{HK}}$ = -4.96 by Hall et al. (2009). Our own measure of solar activity using Ganymede as a proxy yielded S = 0.164 and $\log R'_{\mathrm{HK}}$ = -4.97 (Isaacson & Fischer 2010) for 2009 August 31 when the Sun was still at a low state of its cycle. Thus Kepler-68 is a magnetically inactive star, consistent with its low rotational rate, $v \sin i$ = 0.5 km s^{-1}. Kepler-68 appears to be a middle-aged (age 2-10 Gyr) slowly rotating inactive star, on the main sequence. This is consistent with the age derived from the asteroseismology analysis (Section 6.2).

The activity indices, S and $\log R'_{\mathrm{HK}}$, have modestly lower than solar values, while Figure 1 suggests significantly lower than typical levels of photometric variability compared to the Sun. Hall et al. (2009) summarize 14 years of contemporaneous photometric and spectroscopic (for activity) measurements of 28 solar analog stars with precisions in the photometry capable of detecting changes at roughly half the level seen for the Sun. Although a strong correlation between photometric variability exists with activity, they find that stars with near-solar activity indices show a range of half (not well bounded) to twice solar in photometric variability. Kepler-68 seems consistent with this lower range of photometric change at a given activity level, although not knowing what phase of a Kepler-68 activity cycle was sampled limits fidelity. Multi-year *Kepler* data will eventually enable robust activity – photometric variability understanding.

6.2. *Asteroseismology and the Fundamental Stellar Properties*

The utility of asteroseismology for exoplanet interpretations fundamentally rests on recognizing that both asteroseismic and transit light curve modeling (at high signal to noise levels and with known or assumed eccentricity) provide constraints on the same stellar parameter – $\rho_\star$. Thus high precision knowledge of $\rho_\star$ which commonly results when asteroseismology is feasible provides for a natural means of tightening the exoplanet transit light curve solution by adopting this as a prior – see Gilliland et al. (2011a) and Nutzman et al. (2011). Kepler-68 at Kp = 10.00, near solar temperature, and a KIC radius of 1.06 $R_\odot$ was recognized early as an excellent candidate for asteroseismology with a prediction of 99% chance of success with only two months of short cadence data (Chaplin et al. 2011). Kepler-68 was observed at Short Cadence (SC) (Gilliland et al. 2010) for one month in Q2 as a KASC survey target, then added to the science team SC targets from Q5 onwards to support asteroseismology and fine analyses of the short transit ingress and egress.

The power of asteroseismology in setting estimates of the stellar radius, which determines the exoplanet radius via ratio with the transit depth depending on the square of this ratio, can be seen by recounting knowledge of $R_\star$ for Kepler-68 at the time of initial analyses. Transit light curve solutions for Kepler-68b, with stellar radius as a free parameter returned values of 1.63 $R_\odot$, compared to a KIC radius of 1.06 $R_\odot$ (with spectroscopic solutions favoring something like the KIC value). These two stellar radius values would lead to differences of a factor of 3.6 in the planetary density emphasizing the need for better knowledge of the stellar radius.

Figure 12 shows the Kepler-68 power spectral density with input of 10 months of SC data, the near-evenly spaced peaks characteristic of solar-like oscillations are obvious. Even when first inspecting power spectra from single months of SC data the spacing between modes was trivial to estimate at about 100 μHz compared to a solar value of 135 μHz. Since the mean stellar density is known to scale as the square of frequency spacing (Ulrich 1986), this allowed an early constraint that Kepler-68 was at 0.55 of the solar mean density, and assuming a solar mass (given the solar T_{eff}) provided an estimate of 1.22 $R_\odot$ at the back-of-the-envelope level of analysis.

The high SNR of the power spectrum shown in Figure 12 made peak-bagging (derivation of frequencies for individual modes) straightforward, and eight team members fit the modes using Maximum Likelihood Estimation (MLE), and MCMC approaches (e.g., see Fletcher et al. (2009); Handberg & Campante (2011); Appourchaux et al. (2012)). The adopted frequencies listed in Table 3 came from the single set that most consistently was at the median over all eight.

The fitting technique has been reported in various versions for the analysis of *HST* observations of HD 17156 (Gilliland et al. 2011a), and *Kepler* observations of HAT-P-7 (Christensen-Dalsgaard et al. 2010) and Kepler-10 (Batalha et al. 2011). The underlying stellar evolution modelling is provided using the ASTEC code (Christensen-Dalsgaard 2008a) with eigenfrequency analyses coming from ADIPLS (Christensen-Dalsgaard 2008b).

In the present case the stellar parameters grid includes a few values of the mixing-length parameter α_{ML} in addition to the mass M and the initial composition, characterized by the abundances X and Z by mass of hydrogen and heavy elements. Thus the evolution sequences are characterized by a set of parameters $\{\mathcal{P}_k\} = \{M, Z, X, \alpha_{\mathrm{ML}}\}$. Details of the Kepler-68 grid are presented below.

The fit of a given model to the data is defined in terms of

$$\chi^2_\nu = \frac{1}{N-1} \sum_{i=1}^{N} \left(\frac{\nu_i^{(\mathrm{obs})} - \nu_i^{(\mathrm{mod})}}{\sigma_i} \right)^2 , \qquad (1)$$

where $\nu_i^{(\mathrm{obs})}$ and $\nu_i^{(\mathrm{mod})}$ are the observed and model frequencies and σ_i is the error in the observed frequencies. It is assumed that the degree and order of the observed frequencies have already been determined. In addition, an augmented fit

$$\chi^2 = \chi^2_\nu + \left(\frac{T_{\mathrm{eff}}^{(\mathrm{obs})} - T_{\mathrm{eff}}^{(\mathrm{mod})}}{\sigma(T_{\mathrm{eff}})} \right)^2 , \qquad (2)$$

including the observed and model effective temperature T_{eff} is formed.

For each evolution sequence frequencies are calculated for selected models along the sequence (typically every fifth), but such that frequencies are also available at all models in the sequence in the vicinity of the model $\mathcal{M}'_{\mathrm{min}}$ with the smallest χ^2_ν. Based on homology scaling we then assume that the frequencies in the vicinity of $\mathcal{M}'_{\mathrm{min}}$ can be obtained as $r\nu_i(\mathcal{M}'_{\mathrm{min}})$ where $r = [R/R(\mathcal{M}'_{\mathrm{min}})]^{-3/2}$, R being the surface radius of a model intermediate be-

tween the actual timesteps in the evolution sequence. The best-fitting such model is determined by minimizing

$$\chi_\nu^2(r) = \frac{1}{N-1} \sum_{i=1}^{N} \left(\frac{\nu_i^{(\mathrm{obs})} - r\nu_i(\mathcal{M}'_{\min})}{\sigma_i} \right)^2 \quad (3)$$

as a function of r. The resulting value $r_{\min}$ of r defines an estimate $R_{\min}$ of the radius of the best-fitting model along the given sequence. In this way we ensure that the scaled model is intermediate between two successive timesteps in the evolution sequence for which frequencies have been calculated. Linear interpolation to $R_{\min}$ then defines the final best-fitting model $\mathcal{M}_{\min}(\mathcal{P}_k)$ (which obviously in general does not coincide with a timestep in the evolution sequence) for the given set of model parameters $\{\mathcal{P}_k\}$, and with corresponding $\chi_{\nu,\min}^2(\mathcal{P}_k)$ and $\chi_{\min}^2(\mathcal{P}_k)$. To obtain the final best-fitting model we find the parameter set corresponding to the smallest $\chi_{\nu,\min}^2(\mathcal{P}_k)$ (or $\chi_{\min}^2(\mathcal{P}_k)$) amongst all the evolution sequences. The best-fitting frequencies, e.g., for comparison with the observations are obtained by applying the appropriate scaling $r_{\min}$ to the frequencies of the model $\mathcal{M}'_{\min}$ in the minimizing sequence.

An important goal of the fit is obviously to obtain statistically well characterized estimates of the stellar properties, in particular density, radius, mass and age. In the present analysis these were determined as averages and standard deviations of the properties of the models $\mathcal{M}_{\min}(\mathcal{P}_k)$, over the parameters $\{\mathcal{P}_k\}$, with the weights $\chi_{\min}^{-2}(\mathcal{P}_k)$.

The calculations used the latest OPAL equation of state tables (see Rogers *et al.* 1996) and OPAL opacities at temperatures above 10^4 K (Iglesias & Rogers 1996); at lower temperature the Ferguson *et al.* (2005) opacities were used. Nuclear reactions were calculated using the NACRE parameters (Angulo *et al.* 1999). Diffusion and settling of helium was treated using the Michaud & Proffitt (1993) approximations; diffusion and settling of heavy elements was not taken into account. Convection was treated using the Böhm-Vitense (1958) mixing-length formulation. Although some of the relevant models have a small convective core, core overshoot was not considered.

The spectroscopically determined [Fe/H] $= 0.12 \pm 0.04$ (cf. Section 6.1) is related to the model quantities X and Z by

$$[\mathrm{Fe/H}] = \log \left(\frac{Z/X}{Z_\odot/X_\odot} \right) , \quad (4)$$

where '$\odot$' denotes solar values. To obtain the composition from this one clearly needs to assume a value of $Z_\odot/X_\odot$ and a value of X or a relation between Z and X. For the former the Grevesse & Noels (1993) value of $Z_\odot/X_\odot = 0.0245$ is used. We recognize that substantially lower values have been obtained in more recent solar spectroscopic analyses (see Asplund et al. (2009) and references therein). However, these determinations lead to solar models showing a substantial increase in the discrepancy with the helioseismically determined solar structure (e.g., Bahcall, Serenelli, & Basu (2005), Christensen-Dalsgaard et al. (2009)), compared with models based on the Grevesse & Noels

(1993) composition. Given that the reasons for this discrepancy are so far unknown, we prefer to use as reference a solar composition which provides reasonable agreement with the helioseismic inferences. As a model of Galactic chemical evolution $\Delta Y = 2\Delta Z$ has often been used, and hence (fixing the relation roughly to the Sun), that $X = 0.7679 - 3Z$. The grid in composition allows for a spread in [Fe/H] using models with [Fe/H] $= 0.02$, 0.1 and 0.18, consistent with the [Fe/H] error of 0.074 after inclusion of systematics. With the transformation discussed above this corresponds to $(Z, X) = (0.0183, 0.7130), (0.0217, 0.7029)$ and $(0.0256, 0.6910)$. To avoid being restricted to a specific relation between X and Z we have computed models for all nine resulting combinations of X and Z.

The values of the mixing length have been chosen as $\alpha_{\mathrm{ML}} = 1.5, 1.8$ and 2.1. Models were computed initially between 0.9 and $1.2\,M_\odot$ with a step of $0.02\,M_\odot$. The grid in mass was later refined, with a step of $0.01\,M_\odot$, in the vicinity of the best-fitting models. A total of 282 evolution sequences, with typically $200 - 300$ models in each, are considered in the fit.

The present use of adiabatic frequency calculations, and an inadequate modeling of the near-surface layers, cause errors in the resulting frequencies which must be taken into account in the fit. Here we use a correction to the frequencies for these near-surface errors, of the form

$$\delta\nu = a(\nu/\nu_0)^b \quad (5)$$

(Kjeldsen *et al.* 2008), where $b = 4.90$ is obtained from a corresponding solar fit, $\nu_0 = 2071.33\,\mu\mathrm{Hz}$ was fixed in the middle of the observed frequency range and $a = -1.527\,\mu\mathrm{Hz}$ was obtained from a fit of a suitable reference model to the observed frequencies.

With these procedures, the best-fitting model had $\chi^2 = 5.0$ (cf. Eq. 2). The quality of the fit is illustrated in the échelle diagram (Grec, Fossat & Pomerantz 1983) shown in Fig. 13. The stellar parameters and standard deviations obtained from the weighted averages over the evolution sequences are shown in Table 4.

As a consistency check the global oscillation parameter values $\Delta\nu = 101.51 \pm 0.09\ \mu\mathrm{Hz}$, and $\nu_{\max} = 2154 \pm 13\ \mu\mathrm{Hz}$, were derived from the best-fitting (peak bagging) frequencies and amplitudes of the most prominent peaks providing values quite consistent with estimations from standard, automated detection codes (Hekker et al. (2010), Christensen-Dalsgaard et al. (2010); Verner et al. (2011)). The resulting density, mass and radius provided by grid-based solutions (Basu et al. (2010); Karoff et al. (2010)) were consistent with our more detailed fit presented here. Likewise, fits using the Asteroseismic Modeling Portal (see Metcalfe et al. (2009) for details) gives values very close to those presented here.

Our primary asteroseismic solutions used the formal spectroscopic errors of 44 K on T_{eff} and allowed a spread of ± 0.08 dex on [Fe/H]. We have used grid-based solutions starting with these errors, and the more appropriate errors of 74 K on T_{eff} and 0.074 dex on [Fe/H] to show that changes in the directly constrained stellar density are negligible, and that inferred values of stellar mass and radius change by 0.2 and 0.3 σ respectively in comparison to the errors already quoted in Table 4. The associated errors on stellar properties also changed little

in comparison to values already in use.

The asteroseismic solutions given here are based on only about half of the now available short cadence data. However, the quality of the frequency extractions for Kepler-68 with the data through Q7 only is already sufficiently good that residual errors from the asteroseismic solution are negligible for the inference of exoplanet parameters. Indeed the asteroseismology for Kepler-68 will be among the very best possible with *Kepler*, and further results concentrating on fine details of this star will appear in the future. As an example, some of the best fitting stellar evolution models indicated a small convective core, hence it would be good to explore inclusion of convective core overshoot. Initial exploration of core overshoot indicated that this had negligible impact on the mean stellar density required for exoplanet inferences and was not further pursued. The quality of Kepler-68 data for asteroseismology will likely support inferences on the outer convection zone depth (Mazumdar et al. 2012) and obliquity of the rotation axis (Chaplin et al. 2013) in future analyses.

Kepler-68 is a near twin of α Cen A with inferred values of $T_{\rm eff}$, $R_\star$, $M_\star$, $L_\star$, and age all within 1-σ of each other, despite the small error bars for both – see Bazot, Bourguignon, & Christensen-Dalsgaard (2012) and references therein. Of fundamental parameters only the [Fe/H] differs significantly with α Cen A being more metal rich at 0.24 ± 0.02 (Neuforge-Verheecke & Magain 1997) compared to Kepler-68 at 0.12 ± 0.074. Both stars have now been interpreted with the benefit of asteroseismology. The quality of asteroseismic constraints are superior for Kepler-68, with general astronomical knowledge being better for the nearby binary α Cen A. Differential analyses of these two interesting stars may prove fruitful.

7. PLANET CHARACTERISTICS

7.1. *Fits to photometry and radial velocities*

The physical and orbital properties of both transit signatures are derived by simultaneously fitting *Kepler* photometry and Keck radial velocities and by adopting the mean stellar density, $R_\star$, and $M_\star$ of the host star as determined by asteroseismology.

The *Kepler* photometry and Keck radial velocities are fit with non-interacting Keplerian orbits. The model parameters are the mean stellar density ($\rho_\star$) and a flux and radial velocity zero point and for each planet, the time of transit ($T0$), orbital period (P), impact parameter (b), scaled planetary radius ($R_{\rm P}/R_\star$), radial velocity amplitude (K) and eccentricity and argument of pericenter parametrized as $e\cos(w)$ and $e\sin(w)$. The transit was modeled using the analytic formalization of Mandel & Agol(2002) to fit photometric observations of the transit. We use the quadratic parameterization of limb darkening also described by Mandel & Agol (2002) with coefficients (0.4096, 0.2602) calculated by Claret & Bloemen (2011) for the *Kepler* bandpass. Model fits to the Kepler-68b lightcurve yield an eccentricity that is consistent with zero ($e\cos(w) = 0.02 \pm 0.10$; $e\sin(w) = 20.13 \pm 0.20$) which is consistent with our expectations for tidal circularization (Mazeh 2008). Given the large orbital separation of the outer planet candidate, we can not assume its orbit to be circular based on tidal circularization. The duration of the transit for the outer planet

candidate is consistent with a circular orbit, but the resulting upper limit is still significant ($e \simeq 0.2$). For the remainder of our discussion, the models are constrained to zero eccentricity for both Kepler-68b and Kepler-68c. The radial velocity variations are modeled by assuming non-interacting (Keplerian) orbits. With Kepler-68c validated, the relative inclination between the two orbits is likely less than 20 degrees, as larger relative inclinations would require a fortuitous alignment of the orbital nodes for both planets to transit (Ragozzine & Holman 2010).

We initially fit our observations by fixing $\rho_\star$ to its asteroseismic values (see Section 6.2). Model parameters are found by chi-squared minimization using a Levenberg-Marquardt prescription. We then use the best-fit values to seed a Markov Chain Monte Carlo (MCMC) parameter search (Ford 2005) to fit all model parameters with $\rho_\star$ from the asteroseismic solution. We adopt the asteroseismic determined mean-stellar density as a prior of the overall solution.

7.2. *Transit Timing Variation prospects*

For a nominal two-planet model (i.e., circular orbits with masses from Table 4), the predicted root mean square (RMS) transit timing variations (TTVs) for Kepler-68b & Kepler-68c are both less than half a minute. The median timing uncertainties (based on long-cadence observations) are 3.3 and 20 minutes. Thus, it is not surprising that *Kepler* has not provided a TTV signal due to the interaction of Kepler-68b and Kepler-68c from initial searches. Even with a possible factor of two precision gain from short-cadence data, and an available long time-series providing square root of the number of transits gain, predictions are that detection of a TTV signal on Kepler-68b remains marginal, and unlikely for Kepler-68c. Even increasing the masses of both planets by three times the upper "one-sigma" uncertainty above the estimates in Table 4, the predicted RMS TTVs are less than a minute for both planets. Similarly, even models with unrealistically large eccentricities ($e = 0.3$ and the nominal masses) can result in RMS TTVs of less than a minute. Therefore, we have not performed a detailed TTV analysis of this system.

7.3. *Composition of Kepler-68b*

The synthesis of radial velocity monitoring, transit photometry, and precise asteroseismic stellar characterization reveals that Kepler-68b's mass, radius, and density are all intermediate between the properties of Earth and the Solar System ice giants. Kepler-68b's bulk density ($3.32^{+0.86}_{-0.98}$ g cm^{-3}) is low enough to imply that volatiles (in the form of H/He or astrophysical ices) make a significant contribution to the total planet mass and volume. Kepler-68b cannot be composed of iron and silicates alone; an iron-poor silicate composition is too dense by more than 3 σ. Even a carbon-rich mineralogy – which may lead to solid planets with larger radii than the Earth-like mineralogy often assumed (Madhusudhan, Lee & Mousis 2012) – does not account for the planet density within 1 σ. Following Rogers & Seager (2010) and Rogers et al. (2011), we constrain the range of bulk compositions that are consistent with Kepler-68b's measured mass and radius. Assuming an Earth-like rocky interior composition (consisting of 32% Fe and 68% silicate by mass) Kepler-68b would need between 0.07% and

0.6% of its mass in a H/He gas layer, or alternatively between 21% and 76% of its mass in a water vapor envelope. Intermediate compositions with a mixture of H/He and higher mean molecular weight material from ices are also possible.

Compared to Kepler-68b, the compositions of the other planets orbiting Kepler-68 are less well constrained because the bulk planet densities are unknown. Given its Jupiter-like minimum mass, the outermost planet (Kepler-68d) is likely to be dominated by H/He. Without a transit measurement of Kepler-68d's radius, however, neither the dominant composition nor the more subtle proportion of heavy elements in the planet interior can be directly inferred. At the other extreme of the planetary mass scale, Earth-sized Kepler-68c has only a marginal radial velocity detection. Planet interior structure models place more stringent constraints on the planet mass than the $2\,\sigma$ radial velocity upper limit of 10.6 $M_\oplus$. If Kepler-68c is a rocky body composed of iron and silicate, its mass would fall within 0.65 $M_\oplus < M_p < 2.5\ M_\oplus$ – even a pure iron configuration is allowed. A residual radial velocity precision better than 70 $\mathrm{cm\,s^{-1}}$ is needed to constrain Kepler-68c's make-up.

A striking feature of the Kepler-68 planetary system is that it harbors one of the most strongly irradiated volatile-rich mini-Neptunes detected to date. The stellar energy flux received by Kepler-68b is more than 412 ± 34 times larger than that received by the Earth. Among low-mass ($M_P < 20\ M_\oplus$) planets with measured radii, only Kepler-10b, 55 Cnc e, CoRoT-7b, and Kepler-18b are more strongly irradiated by their host stars. These planets have higher densities than Kepler-68b, however, and are consistent with volatile-less compositions within the $1\,\sigma$ uncertainties on their measured masses and radii. Kepler-10b, CoRoT-7b, and Kepler-18b may be comprised solely of iron and silicates (with no H/He or astrophysical ices), and 55 Cnc e (although not dense enough to have a silicate composition) could have a carbon-rich solid composition without a volatile envelope (Madhusudhan, Lee & Mousis 2012). Kepler-68b's status as the most strongly irradiated mini-Neptune that unambiguously (when the $1\,\sigma$ uncertainties are taken into account) has a significant amount of volatiles makes it a valuable benchmark for planet mass-loss models.

Like many of the highly irradiated *Kepler* planets, mass loss has likely had an important influence sculpting Kepler-68b's composition over its 6.3 Gyr lifetime. Indeed, Kepler-68b lies near the edge of the empirical mass loss destruction threshold noted by several authors (Lecavelier 2007; Ehrenreich & Désert 2011; Jackson, Davis & Wheatley 2012; Lopez, Fortney & Miller 2012). At 8.3 $M_\oplus$, Kepler-68b is close to the minimum mass of 6.5 $M_\oplus$ predicted by mass loss in Lopez, Fortney & Miller (2012). In order to examine the vulnerability of Kepler-68b in greater detail we employed the coupled thermal and mass loss evolution models of Lopez, Fortney & Miller (2012), assuming an Earth-like core and 10% mass loss efficiency.

Although, Kepler-68b is stable against mass loss today, it is possible that it underwent substantial mass loss early in its history when radii were larger and stellar XUV fluxes were over 100× higher (Ribas *et al.* 2005). In fact, if Kepler-68b had a H/He envelope then, it was vulnerable to a type of runaway mass loss that occurs when the mass loss timescale becomes short compared to the cooling timescale (Baraffe et al. 2004; Lopez, Fortney & Miller 2012). Although less than 1% H/He today, Kepler-68b would need to have been ~80% H/He when it was 10 Myr old in order to have a residual primordial H/He envelope today. Moreover, models that undergo this type of extreme mass loss almost always lead to a planet completely stripped of its H/He envelope (Lopez, Fortney & Miller 2012). The initial conditions must be carefully fine tuned in order to arrive at a planet that has such a small but non-zero H/He envelope today. This suggests that it is unlikely that Kepler-68b retains a primordial H/He envelope.

On the other hand, a steam envelope on Kepler-68b should be very stable against mass loss. If Kepler-68b is ~50% water today, then it has only lost ~1% of its initial water envelope since it was 10 Myr old. This suggests that it is possible that like Kepler-68d, 68b formed beyond the snow-line and migrated to its current orbit. However, another distinct possibility is that Kepler-68b does in fact have a H/He envelope, just not a primordial one. Elkins-Tanton & Seager (2008) showed that rocky planets could outgas up to 0.9% of their mass in H/He, more than sufficient to explain the envelope needed today.

On the whole, the Kepler-68 planetary system shares characteristics both with the compact Kepler multi-planet systems (e.g., Kepler-11 and Kepler-20) and with the Solar System. Like Kepler-11 and Kepler-20, Kepler-68 has multiple transiting planets within 0.1 AU. In common with the Solar System, Kepler-68 has a Jovian-mass planet residing outside (at greater orbital separations than) the smaller bodies in the inner system. Between 0.1 and 1.4 AU, there are no confirmed planets in the Kepler-68 system, although our census may be incomplete. The presence of a volatile-rich super Earth within 0.06 AU combined with the presence of a luke-warm Jupiter inside the snow line makes the Kepler-68 system an interesting case study for planet formation and migration theories.

8. SUMMARY

Two distinct sets of transit events were detected in the lightcurve of Kepler-68 constructed from $\sim$ 2 years of *Kepler* photometry. Physical models, constrained by the asteroseismology-derived stellar parameters, were simultaneously fit to the transit light curves and the precision Doppler measurements. Modeling produced tight constraints on the properties of Kepler-68b: $M_P = 8.3^{+2.2}_{-2.4}$ $M_\oplus$, $R_P = 2.31^{+0.06}_{-0.09} R_\oplus$, $\rho_P = 3.32^{+0.86}_{-0.98}$ g cm^{-3}. Evaluation of these properties within a theoretical framework allowed us to draw conclusions about the planet's composition, arguing that a simple iron and silicate structure is excluded. Kepler-68b must retain significant volatiles, even though highly irradiated.

The outer planet, Kepler-68d, is detected only in radial velocities for which an upper limit to the mass is approximately Jupiter in scale, and in a Mars-like orbit. Transits of Kepler-68d would not be expected, if at the same inclination inferred from the impact parameters for Kepler-68b, and Kepler-68c. At the two epochs of *Kepler* data in which transits of Kepler-68d would be seen if they existed, none are present. There is still a 1% chance that if Kepler-68d does transit, the transits could have been

missed in minor data gaps. The presence of an outer giant planet further enriches the interpretive potential for the Kepler-68 system.

Kepler-68c, the intermediate planet, produces transits of only 55 ppm depth (less than 2/3 that of an Earth analog). But due to the brightness of Kepler-68, coupled with low stellar activity and the modest orbital period of 9.6 days, it is detected at high confidence from the *Kepler* photometry. Radial velocities do not provide confirmation, although the formally inferred amplitude at a phase fixed from the transits appears at the 1-σ level. The upper limit on mass from the RVs is not significant for inferring interesting aspects about the planet composition. BLENDER provided a sufficiently high odds ratio to assert tha Kepler-68c is a planet. This validation came with an added complication in this case, however, in that some individual false positive scenarios (the best being for a 7 magnitude fainter background eclipsing binary) provided formally better fits to the phased light curve than did a simple planet transit model. With an odds ratio over 10,000 for the planet interpretation, it is proper to accept this, with perhaps some qualification reserved in this case. Were further data to more definitively provide evidence that a subtle feature at phase 0.5 in the light curve is properly interpreted as a secondary eclipse, then the statistical argument for "validation" would be over-ruled by "confirmation" as a false positive.

This qualifies as an interesting system even in the context of so many exciting and unique discoveries coming from the *Kepler Mission* – with a bright, quiet star providing exquisite asteroseismic constraints on stellar properties; radial velocities providing a precise mass for one transiting planet and supporting discovery of an outer planet; and the second transiting planet validated. That the innermost transiting planet has been shown to have a density intermediate between terrestrial and gas giant planets, with sufficient fidelity to inform theoretical models of its structure, further bolsters the assertion that the Kepler-68 exoplanet system is an important development in this rapidly expanding field.

REFERENCES

Adams, E. R., Ciardi, D. R., Dupree, A. K., Gautier, T. N. III, Kulesa, C., & McCarthy, D. 2012, AJ, 144, 42

Angulo, C., Arnould, M., Rayet, M., Descouvemont, P., Baye, D., et al., 1999, Nucl. Phys. A, 656, 3

Appourchaux, T., Chaplin, W. J., García, R. A., et al. 2012, A&A, 543, A54

Argabright, V.S., VanCleve, J.E., Bachtell, E.E., et al. 2008, Proc. SPIE, 7010, 70102

Asplund, M., Grevesse, N., Sauval, A. J. & Scott, P., 2009, ARA&A, 47, 481

Bahcall, J. N., Serenelli, A. M. & Basu, S., 2005, ApJ, 621, L85

Ballard, S., Fabrycky, D., Fressin, F. et al. 2011, ApJ, 743, 200

Baraffe, I., Selsis, F., Chabrier, G., Barman, T. S., Allard, F., Hauschildt, P.H., Lammer, H. 2004, A&A, 419, L13

Basu, S., Chaplin, W. J., & Elsworth, Y. 2010, ApJ, 710, 1596

Batalha, N.M., Rowe, J.F., Gilliland, R.L., et al. 2010, ApJ, 713, 103

Batalha, N.M., Borucki, W.J., Bryson, S.T., et al 2011, ApJ, 729, 27

Batalha, N. M., Rowe, J. F., Bryson, S. T., et al. 2012, arXiv:1202.5852

Bazot, M., Bourguignon, S., & Christensen-Dalsgaard, J. 2012, MNRAS, 427, 1847

Böhm-Vitense, E., 1958, Z. Astrophys., 46, 108

Borucki, W. J., Koch, D. G., Basri, G., et al. 2011, ApJ, 736, 19

Borucki, W. J., Koch, D. G., Batalha, N. M. et al. 2012, ApJ, 745, 120

Brown, T. M., Latham, D. W., Everett, M. E., & Esquerdo, G. A. 2011, AJ, 142, 112

Caldwell, D. A., Kolodziejczak, J.J., Van Cleve, J. E., et al. 2010a, ApJ, 713, L92

Caldwell, D.A., van Cleve, J.E., Jenkins, J.M., et al. 2010b, Proc. SPIE, 7731, 773117

Chaplin, W. J., Kjeldsen, H., Bedding, T. R., et al. 2011, ApJ, 732, 54

Chaplin, W.J., Sanchis-Ojeda, R., Campante, T. L., et al. 2013, submitted to ApJ

Charbonneau, D., Allen, L. E., Megeath, S. T., et al. 2005, ApJ, 626, 523

Christensen-Dalsgaard, J., 2008a, Astrophys. Space Sci., 316, 13.

Christensen-Dalsgaard, J., 2008b, Astrophys. Space Sci., 316, 113.

Christensen-Dalsgaard, J., Di Mauro, M. P., Houdek, G. & Pijpers, F. 2009, A&A, 494, 205

Christensen-Dalsgaard, J., Kjeldsen, H., Brown, T. M., et al. 2010, ApJ, 713, L164

Christiansen, J. E., Van Cleve, J. E., Jenkins, J. M., et al. 2012, Kepler Data Characteristics Handbook (KSCI-19040-003)

Christiansen, J. E., Jenkins, J. M., Caldwell, D. A., et al. 2012, PASP, 124, 1279

Claret, A.; Bloemen, S.A&A, 529, 75

Désert, J.-M., Lecavelier des Etangs, A., Hébrard, G., Sing, D. K., Ehrenreich, D., Ferlet, R., & Vidal-Madjar, A. 2009, ApJ, 699, 478

Désert, J.-M., Sing, D., Vidal-Madjar, A., et al. 2011, A&A, 526, A12

Désert, J.-M., Charbonneau, D., Fortney, J. J., et al. 2011, ApJ, 197, 11

Eastman, J., Siverd, R., & Gaudi, B. S. 2010, PASP, 122, 935

Ehrenreich, D., & Désert, J.-M. 2011, A&A, 529, A136

Elkins-Tanton, L. T., & Seager, S. 2008, ApJ, 685, 1237

Fazio, G. G., Hora, J.G., Allen, L. E., et al. 2004, ApJS, 154, 10

Ferguson, J. W., Alexander, D. R., Allard, F., Barman, T., Bodnarik, J. G., Hauschildt, P. H., Heffner-Wong, A. & Tamanai, A., 2005, ApJ, 623, 585

Fletcher, S. T., Chaplin, W. J., Elsworth, Y., & New, R. 2009, ApJ, 694, 144

Ford, E. B. 2005, AJ, 129, 1706

Fressin, F., Torres, G., Désert, J.-M. et al. 2011, ApJS, 197, 5

Fressin, F., Torres, G., Rowe, J. F. et al. 2012a, Nature, 482, 195

Fressin, F., Torres, G., Charbonneau, D., Bryson, S. T., Christiansen, J., Dressing, C. D., Jenkins, J. M., Walkowicz, L. M., & Batalha, N. M. 2012b, ApJ, submitted

Gautier, T. N. III, Charbonneau, D., Rowe, J. F. et al. 2012, ApJ, 749, 15

Fröhlich, C., Andersen, B. N., Appourchaux, T., 1997, SolPhys, 170, 1

Gilliland, R. L., & Bohlin, R. 2007, Instrument Science Report ACS 2007-01 (Baltimore, MD: STScI)

Gilliland, R. L., Jenkins, J. M., Borucki, W.J., et al. 2010, ApJ, 713, L160.

Gilliland, R. L., McCullough, P. R., Nelan, E. P., et al. 2011a, ApJ, 726, 2

Gilliland, R. L., Chaplin, W. J., Dunham, E. W., et al. 2011b, ApJS, 197, 6

Grec, G., Fossat, E., & Pomerantz, M. 1983, Solar Phys. 82, 55

Grevesse, N., & Noels, A. 1993, Phys Scr., 133

Hall, J.C., Henry, G.W., Lockwood, G.W., Skiff, B.A., & Saar, S. H. 2009, AJ, 138, 312

Handberg, R., & Campante, T. L. 2011, A&A, 527, A56

Hekker, S., Broomhall, A.-M., Chaplin, W. J., et al. 2010, MNRAS, 402, 2049

Holman, M. J., & Wiegert, P. A. 1999, AJ, 117, 621

Howell, S. B., Everett, M.E., Sherry, W., Horch, E., & Ciardi, D. R. 2011, AJ, 142, 19

Howell, S. B., Rowe, J. F., Bryson, S. T. et al. 2012, ApJ, 746, 123

Huang, X., Bakos, G., & Hartman, J. D. 2013, MNRAS, 429, 2001

Iglesias, C. A. & Rogers, F. J., 1996, ApJ, 464, 943

Isaacson,H., & Fischer, D. A. 2010, ApJ, 725, 875

Jackson, A. P., Davis, T. A., & Wheatley, P. J. 2012, MNRAS, 422, 2024

Jenkins, J. M., Caldwell, D. A., Chandrasekaran, H., et al. 2010a, ApJ, 713, L87

Jenkins, J. M., Caldwell, D. A., Chandrasekaran, H., et al. 2010b, ApJ, 713, L120

Jenkins, J. M., Chandrasekaran, H., McCauliff, S. D., et al. 2010c, Proc. SPIE, 7740, 77400D

Johnson, J. A., Winn, J. N., Albrecht, S., Howard, A. W., Marcy, G. W., & Gazak, J. Z. 2009, PASP, 121, 1104

Karoff, C., Chaplin, W. J., Appourchaux, T., et al. 2010, Astron. Nachr., 331, 972

Kjeldsen, H., Bedding, T. R. & Christensen-Dalsgaard, J., 2008, ApJ, 683, L175

Knutson, H. A., Charbonneau, D., Allen, L. E., Burrows, A., & Megeath, S. T. 2008, ApJ, 673, 526

Lecavelier Des Etangs, A. 2007, A&A, 461, 1185

Lissauer, J. J., Fabrycky, D. C., Ford, E. B. et al. 2012, Nature, 470, 53

Lissauer, J. J.,et al. 2013, in preparation

Lockwood, G.W., Skiff, B.A., Henry, G.W., Henry, S., Radick, R. R., Baliunas, S. L., Donohue, R. D., & Soon, W. 2007, ApJS, 171, 260

Lopez, E. D., Fortney, J. J., & Miller, N. K. 2012, ApJ, 761, 59

Lucas, P. W., & Samuel, D. 2009, Proc. Int. Astr. Union, 5, 779

Madhusudhan, N., Lee, K. K. M., & Mousis, O. 2012, ApJ, 759, L40

Mandel, K. & Agol, E., 2002, ApJ, 580, 171

Mandushev, G., Torres, G., Latham, D. W., et al. 2005, ApJ, 621, 1061

Marcy, G. W., Butler, R. P., Vogt. S. S., et al. 2008, Physica Scripta Volume T, 130, 014001

Mazeh, T. 2008, in Tidal Effects in Stars, Planets and Disks, EAS Publications Series, eds. M.-J. Goupil & J.-P. Zahn (EDP Sciences), Vol. 29, p. 1

Mazumdar, A., Monteiro, M. J. P. F. G., Ballot, J., et al. 2012, AN, 333, 1040

Metcalfe, T.S., Creevey, O. L. & Christensen-Dalsgaard, J. 2009, ApJ, 699, 373

Michaud, G. & Proffitt, C. R., 1993, In *Proc. IAU Colloq. 137: Inside the stars*, eds Baglin, A. & Weiss, W. W., Astronomical Society of the Pacific Conference Series, San Francisco, 40, 246

Morton, T. D., & Johnson, J. A. 2011, ApJ, 738, 170

Morton, T. D. 2012, ApJ, 761, 6 (arXiv:1206.1568)

Neuforge-Verheecke, C., & Magain, P. 1997, A&A, 328, 261

Nutzman, P., Gilliland, R. L., McCullough, P. R., et al. 2011, ApJ, 726, 3

Ofir, A., & Dreizler, S. 2012, arXiv:1206.5347

Prsa, A. 2010, http://astro4.ast.villanova.edu/aprsa/

Queloz, D., Henry, G. W., Sivan, J. P., et al. 2001, A&A, 379, 279

Ragozzine, D., Holman, M. J. 2010, arXiv:1006.3727

Ribas, I., Guinan, E. F., Güdel, M., & Audard, M. 2005, ApJ, 622, 680

Robin, A. C., Reylé, C., Derriére, S., & Picaud, S. 2003, A&A, 409, 523

Rogers, F. J., Swenson, F. J. & Iglesias, C. A., 1996, ApJ, 456, 902

Rogers, L. A., Bodenheimer, P., Lissauer, J. J., & Seager, S. 2011, ApJ, 738, 59

Rogers, L. A., Seager, S. 2010, ApJ, 716, 1208

Slawson, R. W., Prša, A., Welsh, W. F. et al. 2011, AJ, 142, 160

Smith, J. C., Stumpe, M. C., Van Cleve, J. E., et al. 2012, PASP, 124, 1000

Stumpe, M. C., Smith, J. C., Van Cleve, J. E., et al. 2012, PASP, 124, 985

Torres, G., Konacki, M., Sasselov, D. D., & Jha, S. 2004, ApJ, 614, 979

Torres, G., Konacki, M., Sasselov, D. D., Jha, S. 2005, ApJ, 619, 558

Torres, G., Fressin, F., Batalha, N. M., et al. 2011, ApJ, 727, 24

Torres, G., Fischer, D.A., Sozzetti, A., Buchhave, L. A., Winn, J. N., Holman, M. J., & Carter, J. A. 2012, ApJ, 757, 161

Twicken, J. D., Clarke, B. D., Bryson, S. T., et al. 2010, Proc. SPIE, 7740, 774023

Twicken, J. D., Chandrasekaran, H., Jenkins, J. M., Gunter, J. P., Girouard, F., Klaus, T. C. 2010, Proc. SPIE, 7740, 77401U

Ulrich, R. K. 1986, ApJ, 306, L37

Valenti, J. A., & Piskunov, N. 1996, A&AS, 118, 595

Valenti, J. A., & Fischer, D. A. 2005, ApJS, 159, 141

Van Cleve, J., & D. A. Caldwell 2009, Kepler Instrument Handbook, KSCI 19033-001, (Moffett Field, CA: NASA Ames Research Center)

Verner, G. A., Elsworth, Y., Chaplin, W. J., et al. 2011, MNRAS, 415, 3539

Vogt, S. S., Allen, S. L., Bigelow, B. C., et al. 1994, Proc. SPIE, 2198, 362

Werner, M. W., Roellig, T. L., Low, F. J., et al. 2004, ApJS, 154, 1

TABLE 1
Direct and Difference Image values for Kepler-68b and Kepler-68c

Row	Direct				Difference Kepler-68b				Difference Kepler-68c			
Column	943	944	945	946	943	944	945	946	943	944	945	946
343	.000	*.003*	*.001*	.000	+.000	*+.160*	*+.000*	+.000	-.004	*-.026*	*+.000*	+.001
342	.003	.111	.099	.002	+.003	-.004	+.163	+.001	-.013	+.000	+.286	+.008
341	.005	.120	.111	.015	+.006	+.048	-.002	+.011	-.005	-.078	-.005	+.035
340	.009	.124	.124	.017	+.008	+.008	+.010	+.017	-.002	-.013	+.020	+.037
339	.003	.111	.124	.010	+.002	+.257	+.217	+.008	+.002	+.169	+.385	+.021
338	.000	.001	.003	.003	+.000	+.002	+.009	+.003	+.004	+.002	+.018	-.005

NOTE. — Column and row values refer to pixels on channel 59 of the *Kepler* detectors for Quarter 9. The Direct image has been normalized by the total electrons per cadence of 2.4×10^9. The difference images have been normalized by the same factor scaled by the known depths of 346 and 53 ppm for Kepler-68b and Kepler-68c respectively. For internal consistency the sums over these normalized difference images should be $\sim$1 (this is satisfied). Kepler-68 is nearly centered in these tabular domains, while KIC 11295432 (7 magnitudes fainter companion – see text) is near center of row 343, and columns 944–945 pixels as italicized in entries. Typical uncentainties for Kepler-68b entries are 0.004, and 0.04 for Kepler-68c.

TABLE 2
Relative Radial Velocities and Line Bisectors for Kepler-68

HJD -2450000	RV (m s^{-1})	RV$_e$ (m s^{-1})	bs (m s^{-1})	bs$_e$ (m s^{-1})
5313.082	3.98	2.1	6.1	1.8
5319.109	0.00	2.3	-10.7	2.7
5322.051	-2.75	1.9	-2.1	1.8
5372.983	-1.27	1.9	17.3	2.5
5377.929	-0.39	1.9	-2.5	4.4
5381.000	-7.85	2.0	4.5	2.8
5396.963	-5.20	2.1	-7.7	1.4
5400.020	0.14	3.4	-3.1	2.7
5412.923	-8.94	1.9	9.6	3.9
5426.913	-6.81	1.9	-3.9	3.7
5431.784	-1.04	1.9	-8.4	3.3
5434.873	-14.06	1.7	7.0	3.5
5435.931	-9.75	2.0	2.3	3.5
5436.971	-8.34	1.9	-3.9	3.0
5437.945	-4.90	1.8	3.1	2.3
5438.996	-6.18	1.8	4.8	2.0
5439.928	-10.42	1.7	9.8	1.8
5440.975	-10.20	1.7	-7.6	1.2
5455.810	-12.90	2.0	-3.8	1.5
5490.830	-8.52	2.0	-2.0	3.0
5672.026	27.25	1.9	-3.5	3.5
5672.998	23.74	2.0	1.6	3.1
5673.996	28.12	2.0	6.5	2.1
5696.974	30.91	2.0	11.1	2.2
5697.964	33.04	2.1	9.2	1.8
5698.962	26.37	2.0	13.0	1.2
5722.995	31.84	2.0	-5.9	3.0
5724.034	36.50	2.1	-10.0	2.4
5728.901	32.98	2.1	3.2	2.2
5734.064	34.50	2.0	-5.3	2.2
5734.951	35.37	2.0	-3.7	2.7
5735.975	33.84	2.0	2.7	1.3
5739.034	33.61	2.0	0.8	1.8
5751.797	27.85	2.1	-14.9	2.5
5752.105	27.06	2.0	-10.2	2.5
5752.779	25.05	2.0	-2.8	1.4
5759.975	27.91	2.0	15.1	1.7
5761.076	30.96	1.9	-6.6	2.9
5761.842	24.79	2.0	-0.7	1.8
5763.033	28.05	2.0	-9.7	1.4
5763.851	24.13	2.0	-10.1	2.6
5782.908	24.68	2.0	2.5	2.0
5795.024	16.72	2.2	-8.7	1.6
5814.736	22.27	1.9	9.0	2.7
6077.045	-6.84	2.0	-10.0	1.7
6098.094	-2.72	2.1	-4.9	1.5
6098.829	-3.40	2.0	-5.2	1.8
6102.008	3.17	2.0	18.4	1.9
6114.872	-6.21	2.0	-0.4	2.3
6145.875	-0.55	2.1	10.2	2.0
6148.929	5.57	1.9	1.8	1.3
6151.061	-1.64	2.0	-1.7	1.5

TABLE 3
MEASURED FREQUENCIES ν_{nl} OF KEPLER-68 (IN μHz).

n	$l = 0$	$l = 1$	$l = 2$
14	–	1661.02 ± 0.35	–
15	1668.43 ± 0.29	1713.38 ± 0.15	1761.36 ± 0.32
16	1767.09 ± 0.29	1813.49 ± 0.19	1861.58 ± 0.37
17	1867.94 ± 0.17	1914.65 ± 0.20	1962.99 ± 0.20
18	1969.08 ± 0.14	2016.27 ± 0.11	2064.85 ± 0.11
19	2070.73 ± 0.09	2117.70 ± 0.07	2166.32 ± 0.23
20	2172.02 ± 0.13	2219.40 ± 0.14	2268.08 ± 0.20
21	2273.37 ± 0.15	2321.09 ± 0.14	2369.55 ± 0.60
22	2375.43 ± 0.25	2423.57 ± 0.29	2472.54 ± 0.64
23	2477.86 ± 0.36	2525.73 ± 0.30	–

TABLE 4
Star and planet parameters for the Kepler-68 system.

Parameter	Value	Notes
Transit and orbital parameters: Kepler-68b		
Orbital period P (days)	5.398763 ± 0.000004	A
Midtransit time E (BJD)	$2455006.85729 \pm 0.00042$	A
Scaled semimajor axis $a/R_\star$	10.68 ± 0.14	A
Scaled planet radius $R_{\rm P}/R_\star$	0.01700 ± 0.00046	A
Impact parameter b	0.45 ± 0.17	A
Orbital inclination i (deg)	87.60 ± 0.90	A
Orbital semi-amplitude K (m s^{-1})	2.63 ± 0.71	B
Orbital eccentricity e	0	B
Center-of-mass velocity γ (km s^{-1})	-20.9 ± 0.1	B
Transit and orbital parameters: Kepler-68c		
Orbital period P (days)	9.605085 ± 0.000072	A
Midtransit time E (HJD)	2454969.3805 ± 0.0041	A
Scaled semimajor axis $a/R_\star$	15.68 ± 0.20	A
Scaled planet radius $R_{\rm P}/R_\star$	0.00703 ± 0.00025	A
Impact parameter b	0.84 ± 0.11	A
Orbital inclination i (deg)	86.93 ± 0.41	A
Orbital semi-amplitude K (m s^{-1})	$1.25^{+0.65}_{-0.95}$	B
Observed stellar parameters		
Effective temperature $T_{\rm eff}$(K)	5793 ± 74	C
Spectroscopic gravity $\log g$(cgs)	4.281 ± 0.06	C
Metallicity [Fe/H]	$+0.12 \pm 0.074$	C
Projected rotation $v \sin i$(km s^{-1})	0.5 ± 0.5	C
Fundamental Stellar Properties		
Density $\rho_\star$ (g cm^{-3})	0.7903 ± 0.0054	D
Mass $M_\star(M_\odot)$	1.079 ± 0.051	D
Radius $R_\star(R_\odot)$	1.243 ± 0.019	D
Surface gravity $\log g_\star$ (cgs)	4.281 ± 0.008	D
Luminosity $L_\star$ ($L_\odot$)	1.564 ± 0.141	D
Absolute V magnitude M_V (mag)	4.34 ± 0.09	D
Age (Gyr)	6.3 ± 1.7	D
Distance (pc)	135 ± 10	D
Planetary parameters: Kepler-68b		
Mass $M_{\rm P}$ ($M_\oplus$)	$8.3^{+2.2}_{-2.4}$	A,B,C,D,F
Radius $R_{\rm P}$ ($R_\oplus$)	$2.31^{+0.06}_{-0.09}$	A,B,C,D
Density $\rho_{\rm P}$ (g cm^{-3})	$3.32^{+0.86}_{-0.98}$	A,B,C,D,F
Surface gravity $\log g_{\rm P}$ (cgs)	3.14 ± 0.11	A,B,C,D,F
Orbital semimajor axis a (AU)	0.06170 ± 0.00056	E
Equilibrium temperature $T_{\rm eq}$ (K)	1280 ± 90	G
Planetary parameters: Kepler-68c		
Mass $M_{\rm P}$ ($M_\oplus$)	$4.8^{+2.5}_{-3.6}$	A,B,C,D,F
Radius $R_{\rm P}$ ($R_\oplus$)	$0.953^{+0.037}_{-0.042}$	A,B,C,D
Density $\rho_{\rm P}$ (g cm^{-3})	$28.^{+13.}_{-23.}$	A,B,C,D,F
Orbital semimajor axis a (AU)	0.09059 ± 0.00082	E
Planetary parameters: Kepler-68d		
Orbital period P (days)	580 ± 15	F
Minimum mass $M_P \sin i$ (M_J)	0.947 ± 0.035	D,F
Orbital semi-amplitude K (m s^{-1})	19.9 ± 0.75	D,F
Orbital semimajor axis a (AU)	1.40 ± 0.03	D,F
Orbital eccentricity e	0.18 ± 0.05	F

Note. — A: Based primarily on an analysis of the photometry,
B: Based on a joint analysis of the photometry and radial velocities,
C: Based on an analysis by D. Fischer of the Keck/HIRES template spectrum using SME (Valenti & Piskunov 1996),
D: Based on asteroseismology analysis,
E: Based on Newton's revised version of Kepler's Third Law and the results from D,
F: Based on radial velocities,
G: Calculated assuming a random distribution of Bond albedo over 0.0 to 0.5, and a random set ranging from zero to full redistribution of heat from day to night sides.
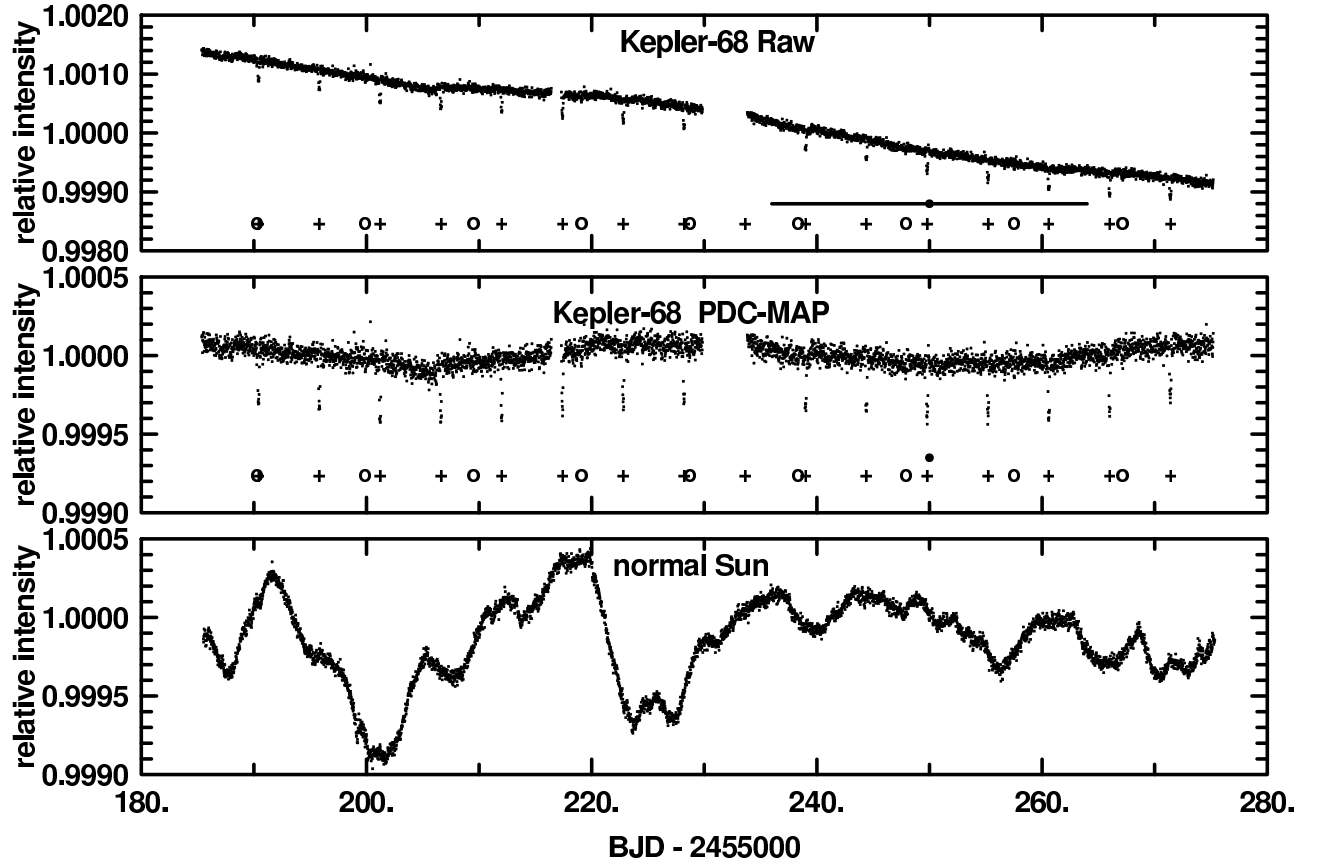
FIG. 1.— Top panel shows the raw flux (SAP_FLUX) time series for Kepler-68, after normalization by the median for the representative quarter Q4. The plus signs flag central times of transits of Kepler-68b, while the open circles flag transits of Kepler-68c. The solid dot shows the expected position for a transit of the outer, RV-detected Kepler-68d with the horizontal bar showing the 1-σ phase uncertainty – no transit is seen. PDC-MAP corrected flux time series produced by the *Kepler* photometry pipeline (PDCSAP_FLUX) is shown in the middle panel. The lower panel shows a 90-day segment of SOHO VIRGO/SPM (Fröhlich et al. 1997) data from the green channel scaled as discussed in Gilliland et al. (2011b) to match the *Kepler* bandpass. The solar data centered on 2005.52 were taken from a period of average variability.

Gilliland *et al.*
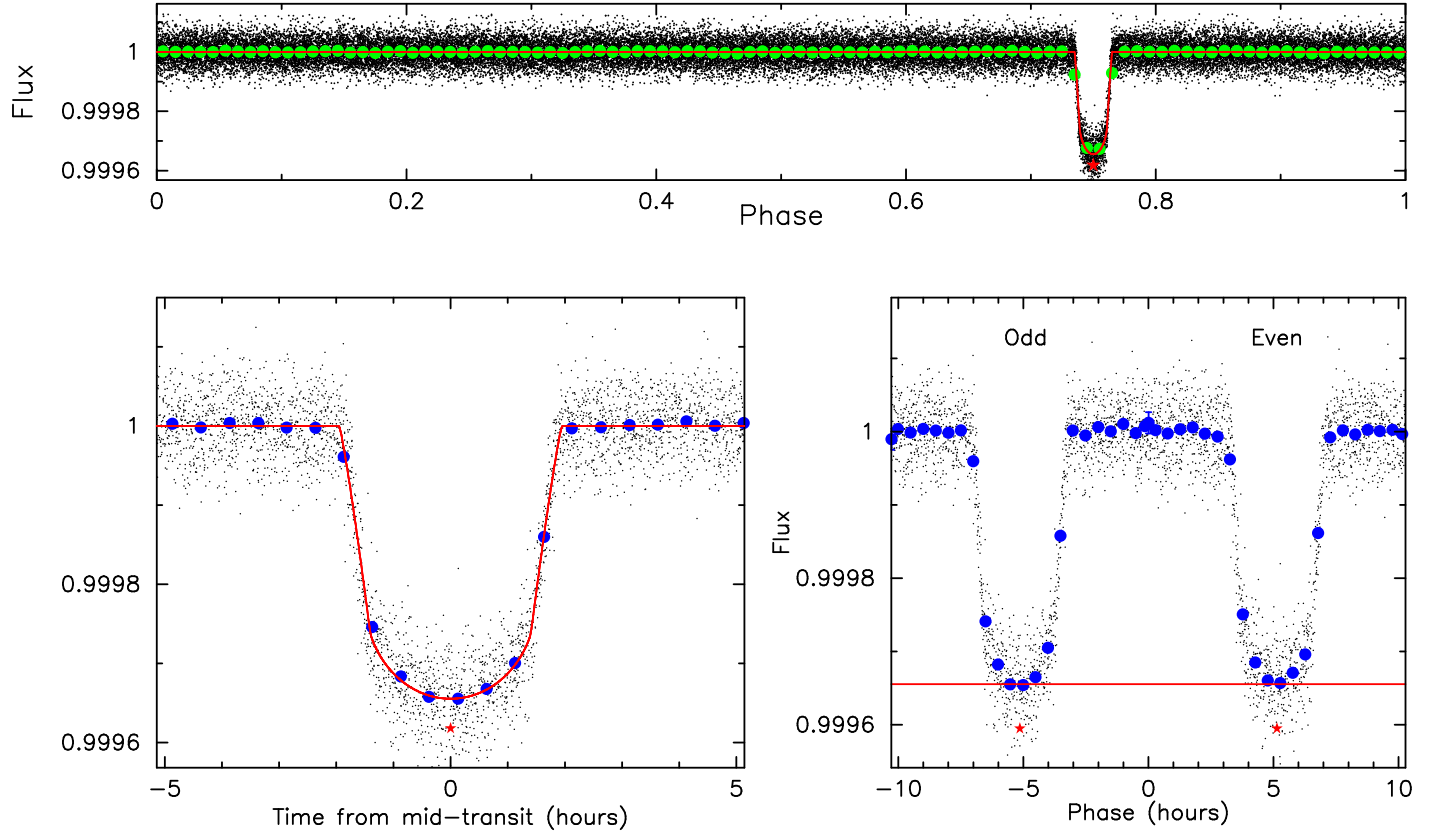
FIG. 2.— The upper panel shows the de-trended time series over Q1-Q11 (without Q3 as discussed in the text) after folding on the 5.39877 day period of Kepler-68b such that the transit falls at phase 0.75. The signal for Kepler-68c has also been subtracted. Green points show the data binned in 0.01 phase intervals, the red line is the best fitting transit model. The lower left panel provides detail on the phased and folded light curve at the position of the transit; solid dots indicate 30-minute averages and the solid line is the best fitting transit light curve fit. The lower right panel details Odd and Even numbered transits individually co-added. Red stars mark center-of-transit times.
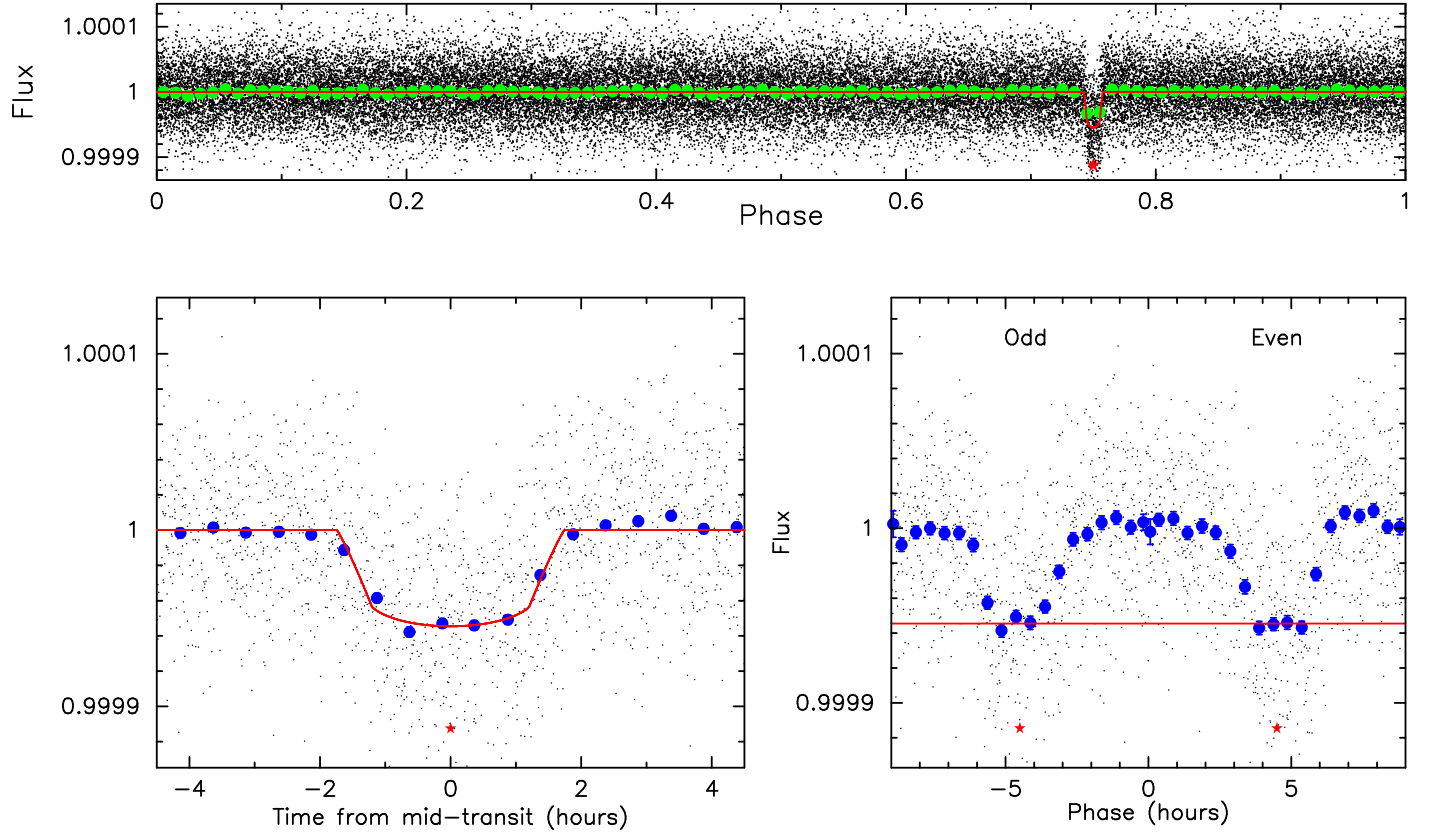
FIG. 3.— Same as Figure 2, but for Kepler-68c after removal of the Kepler-68b transits.
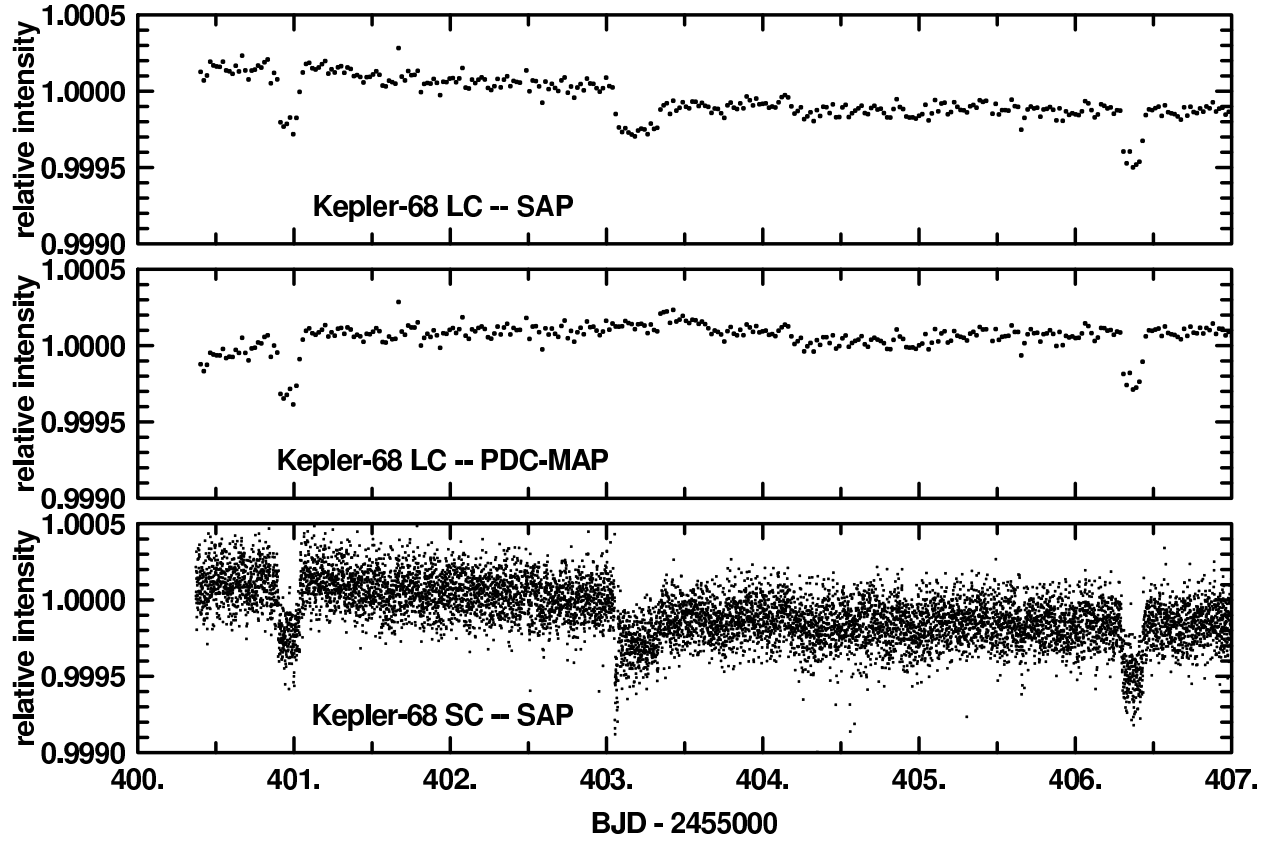
Fig. 4.— The upper panel shows raw *Kepler* long cadence data spanning six days centered on the "monotransit" event shown in Fig. 3 of Ofir & Dreizler (2012). The middle panel shows the same data after pipeline processing with PDC-MAP. The lower panel shows the same time period with short cadence raw data.
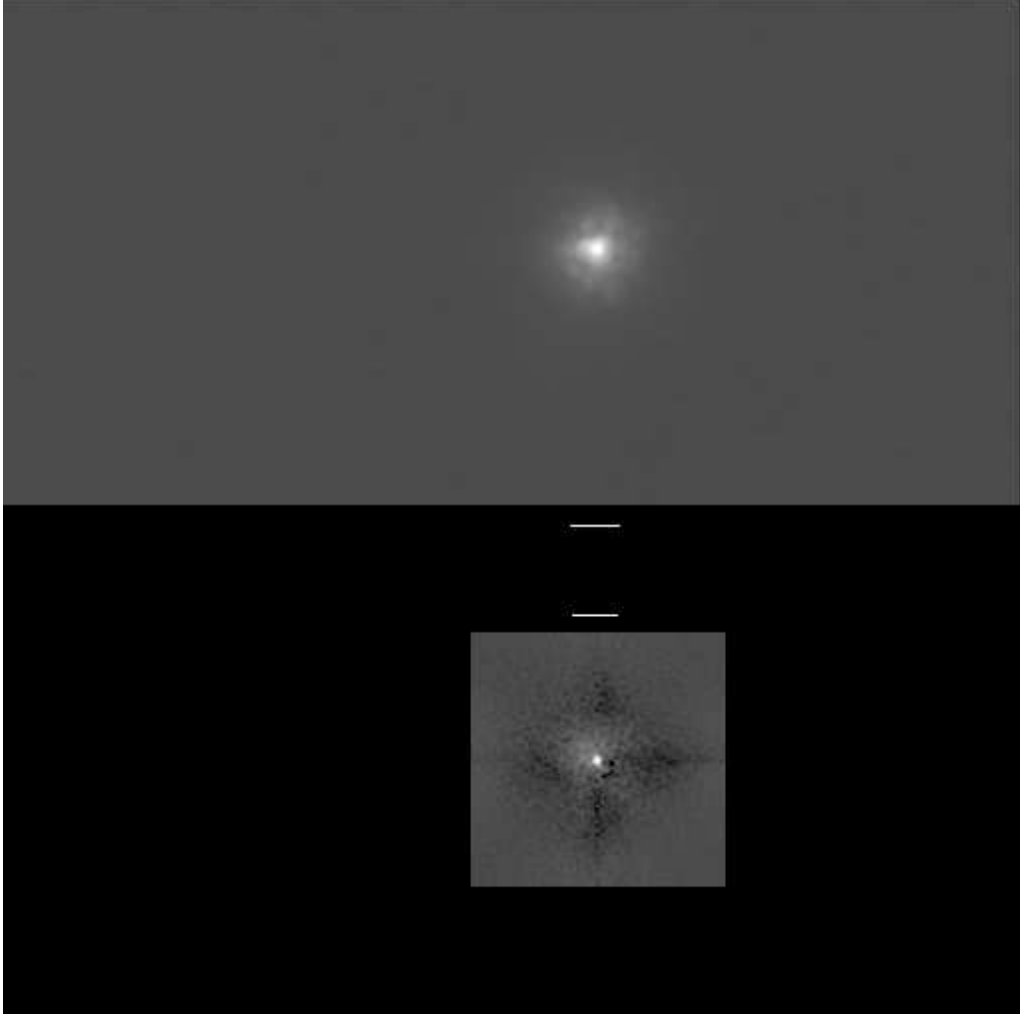
FIG. 5.— The upper panel shows a $10\rlap{.}''6$ by $5''$ region of the ARIES Ks band AO image. The lower panel shows the full $2\rlap{.}''76$ square R-band Speckle image. Bars next to images illustrate $0\rlap{.}''5$ scale. Both images have been normalized to a common central intensity, offset with a positive zero point of 1% of full scale and then displayed with identical logarithmic stretches. The speckle image is superior for resolution, with the AO being better both in terms of field of view and limiting depth.
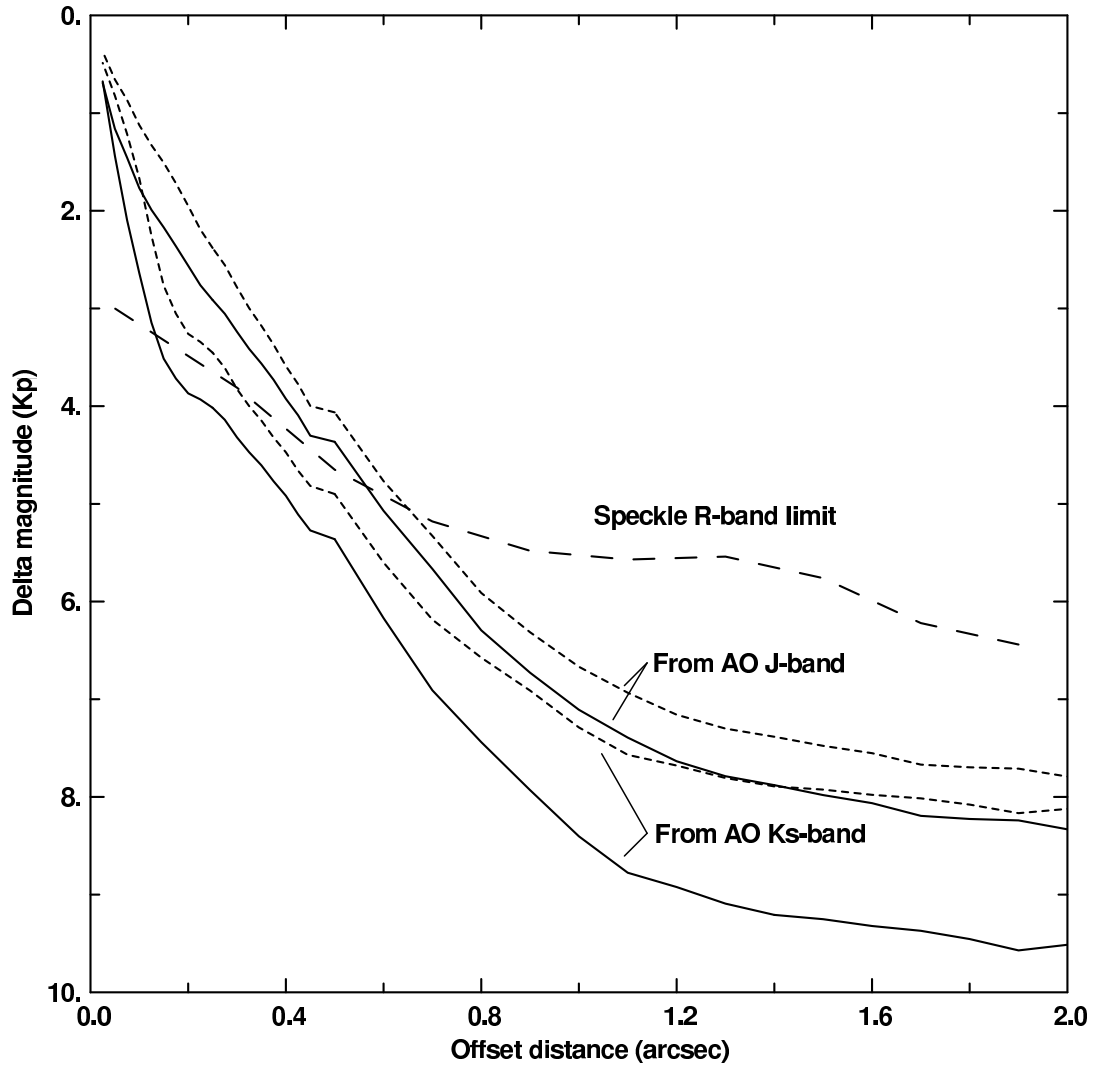
FIG. 6.— Limiting depths provided from the ARIES AO, and speckle imaging as a function of offset distance. The short dashed lines show the direct *J* and *Ks* limits from ARIES with the associated solid curves being the estimated *Kp* limits using the Appendix A transformations from Howell et al. (2011). The long dashed line shows the *R*-band limit from WIYN speckle observations, which has a central wavelength very similar to the *Kepler* bandpass.
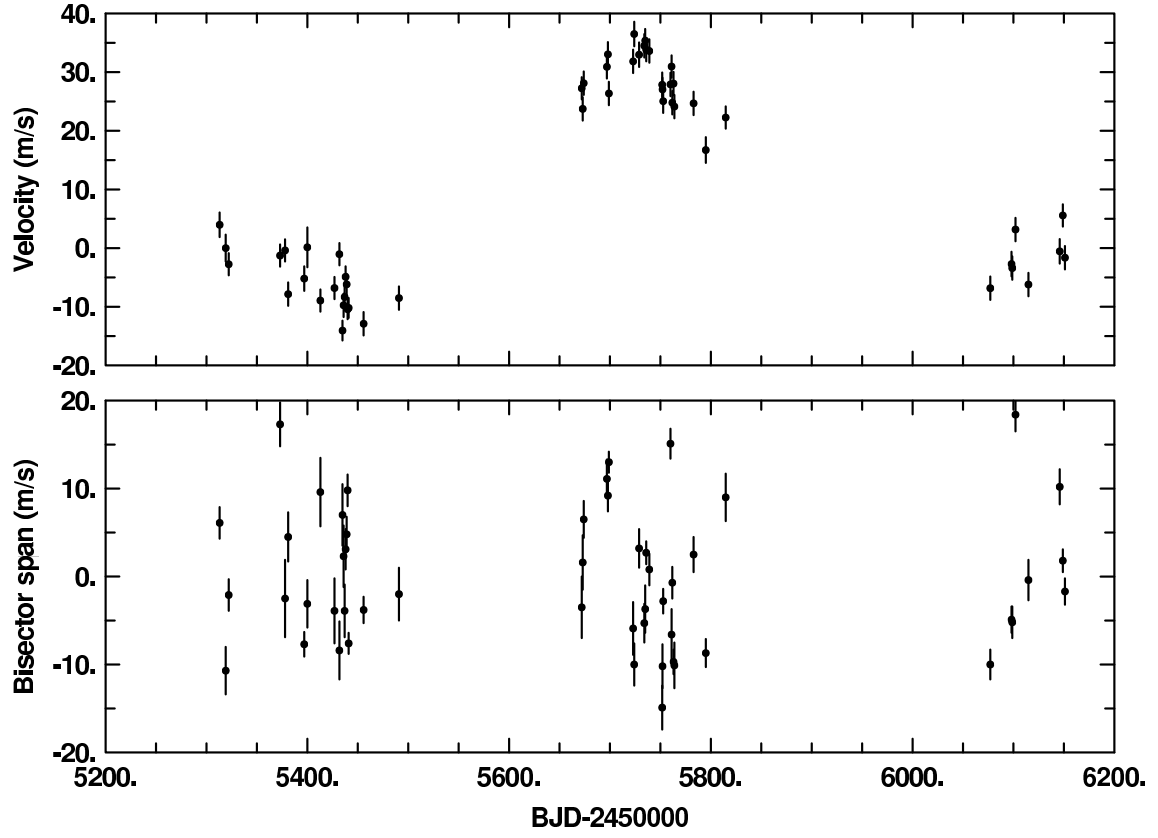
FIG. 7.— Radial velocities versus time from the Keck-HIRES spectra over 2010-2012 are shown in the upper panel. Error bars include the internal uncertainties and the expected combined astrophysical and instrumental jitter of 1.5 m s^{-1}, added in quadrature. The lower panel shows line bisectors derived from the same spectra.
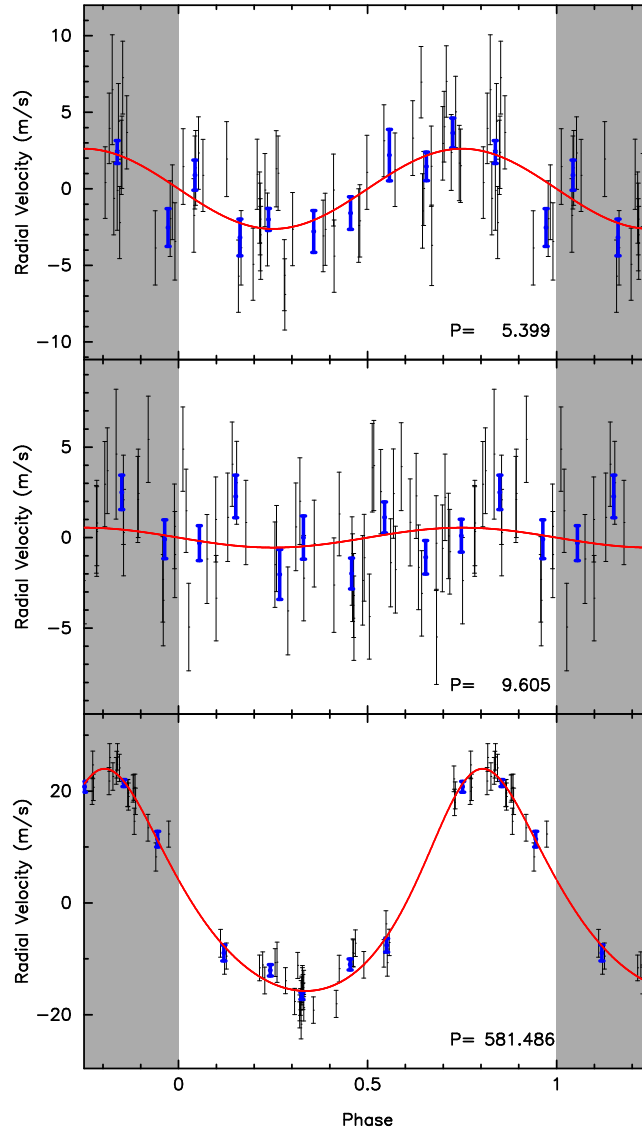
FIG. 8.— This figure shows the radial velocity measurements and model fits. The top panel shows the RV measurements and model phase folded to the orbital period of Kepler-68b. The black lines show the radial velocity measurements and 1-σ uncertainties after the removal of the best fit model for Kepler-68c and Kepler-68d. The thick blue points show the same RV data but averaged in 0.1 phase bins. The red line is the best fit Keplerian orbital model. The orbital period is indicated in the lower right portion of the panel. The middle and bottom panels show the RV measurements in similar fashion for Kepler-68c and Kepler-68d respectively. The fits for Kepler-68b and Kepler-68c have eccentricity forced to zero, while the Kepler-68d solution allowed this as a parameter.
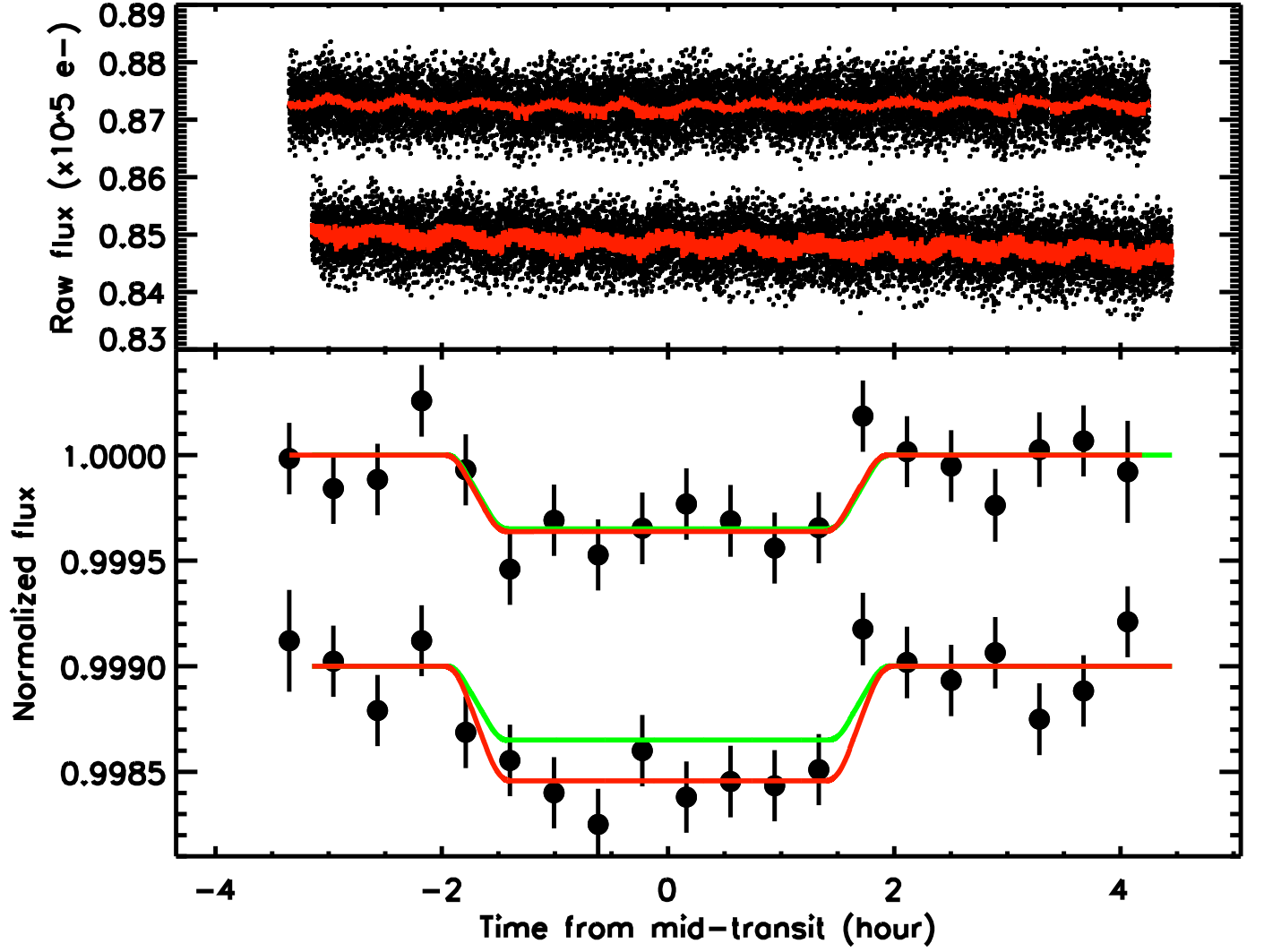
FIG. 9.— *Spitzer* transit light-curves of Kepler-68b observed in the IRAC band-pass at 4.5 μm. Top panel : raw (unbinned) transit light-curves for the two visits of Kepler-68b. The second visit (at the bottom) is shifted vertically from the first visit (at the top) for display purpose. The red solid lines correspond to the best fit model which include the time and position instrumental decorrelations as well as the model for the planetary transit (see text). Bottom panel : corrected, normalized, and binned by 23 minutes transit light-curves with the transit best-fit plotted in red and the transit shape expected from the *Kepler* observations overplotted as a green line. The second visit has again been shifted down for display.
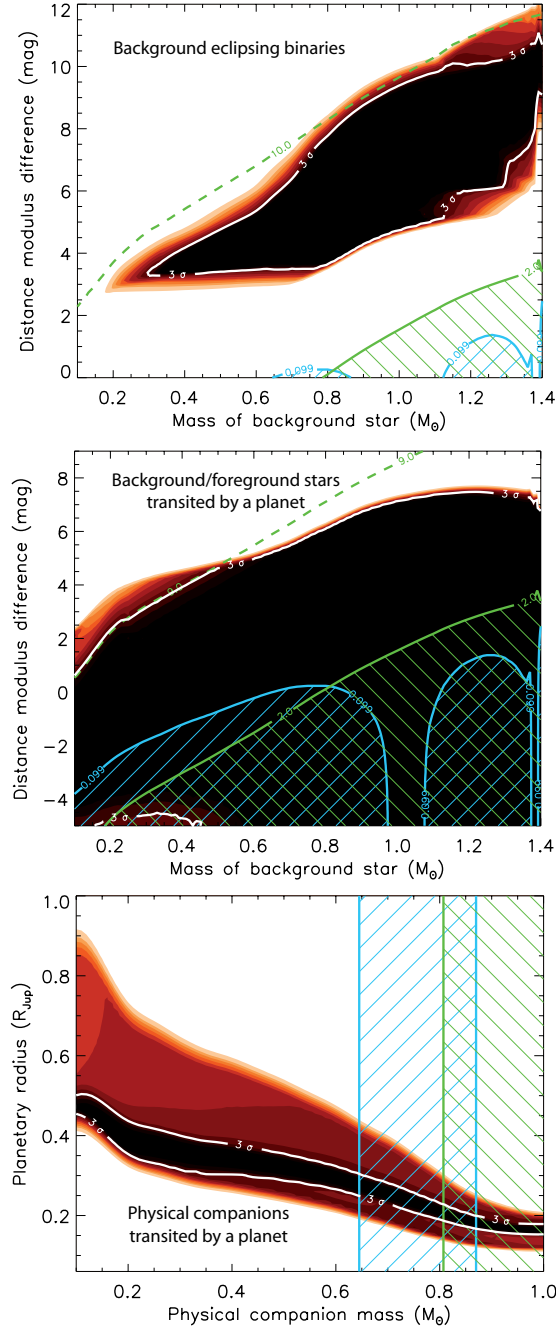
FIG. 10.— BLENDER goodness-of-fit contours for Kepler-68c corresponding to the three different scenarios that contribute to the overall blend frequency: background eclipsing binaries (top), background or foreground stars transited by a planet (middle), and physical companions transited by a planet (bottom). Only blends inside the solid white contours produce light curves matching the *Kepler* photometry within acceptable limits (3σ, where σ is the significance level of the χ^2 difference compared to a transit model fit; see Fressin et al. 2011). Lighter-colored areas (red, orange, yellow) mark regions of parameter space giving increasingly worse fits to the data (4σ, 5σ, etc.), and correspond to blends we consider to be ruled out. The axes in each panel represent two of the dimensions of parameter space for blends. For the top two diagrams the vertical axis represents the distance between the background/foreground star and the target, expressed here in terms of a difference in distance modulus rather than in parsecs. The horizontal axis corresponds to the mass (spectral type) of the intruding star. In the lower panel (physically bound scenarios) the vertical axis is the size in Jupiter radii of the planet transiting the companion star. The cyan cross-hatched areas indicate regions of parameter space ruled out because the resulting $r - K_s$ color of the blend is either too red (left) or too blue (right) compared to the measured color, by more than 3σ (0.10 mag). In the top and middle panels the solid green line is a line of constant magnitude difference ($\Delta Kp = 2$) between the target and the background star. Blends involving stars brighter than this (which lie lower in the diagram) would have been detected in our spectroscopic observations (see Sect. 6.1), and are thus ruled out. This is indicated by the cross-hatched regions below the green lines. Finally, the dashed green lines in the top two panels are roughly parallel to the solid green lines, and are also lines of constant magnitude difference between the target and a background star. They correspond to the faintest blends that can mimic the transit: approximately $\Delta Kp = 10$ for background eclipsing binaries (top), and $\Delta Kp = 9$ for background/foreground stars transited by a planet (middle).
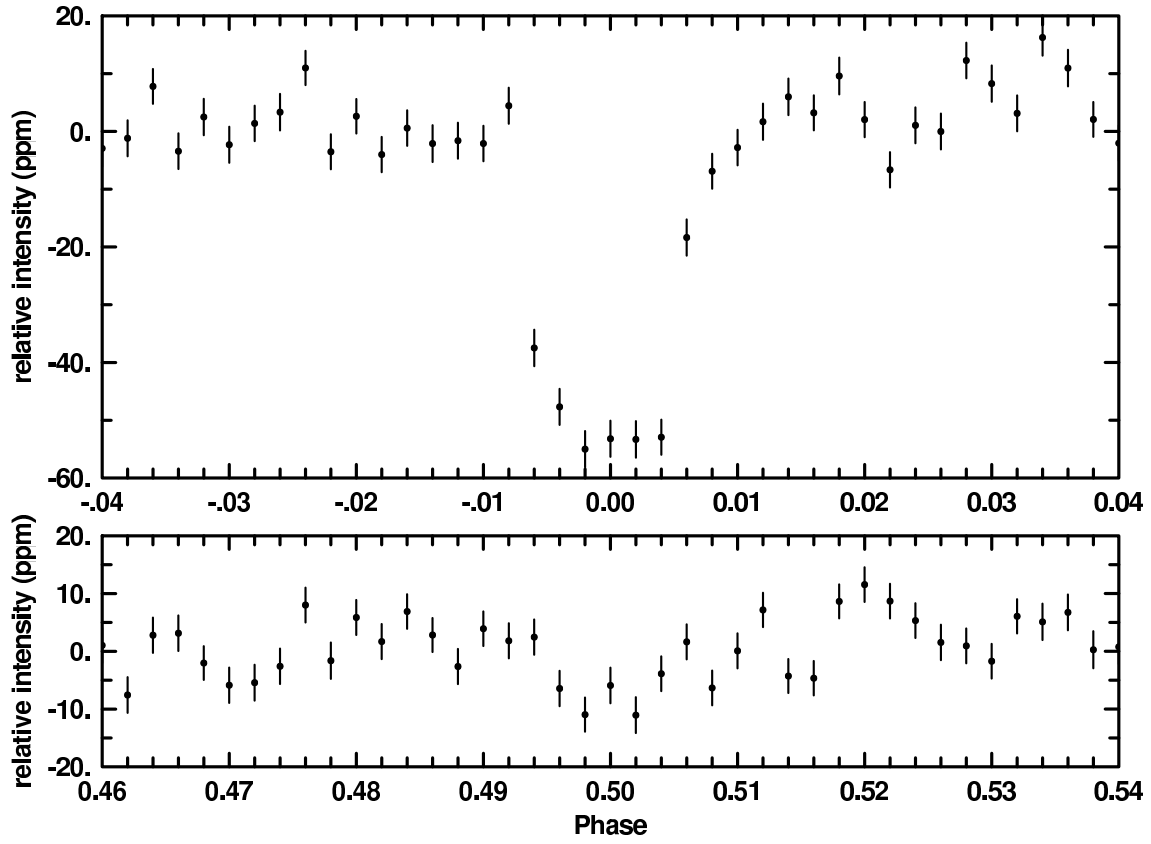
FIG. 11.— The short cadence data for Kepler-68c phased onto the orbital period. The upper panel shows the transit centered at phase zero. The error bars show the formal error per 0.002 phase bin evaluated as standard deviation divided by square root of the number of contributing points. The lower panel shows the phased data exactly 0.5 out of phase from the transit and illustrates the subtle evidence of a secondary eclipse that the BLENDER analysis locks onto in providing some false positive scenarios with a formally higher significance than a simple transit fit.
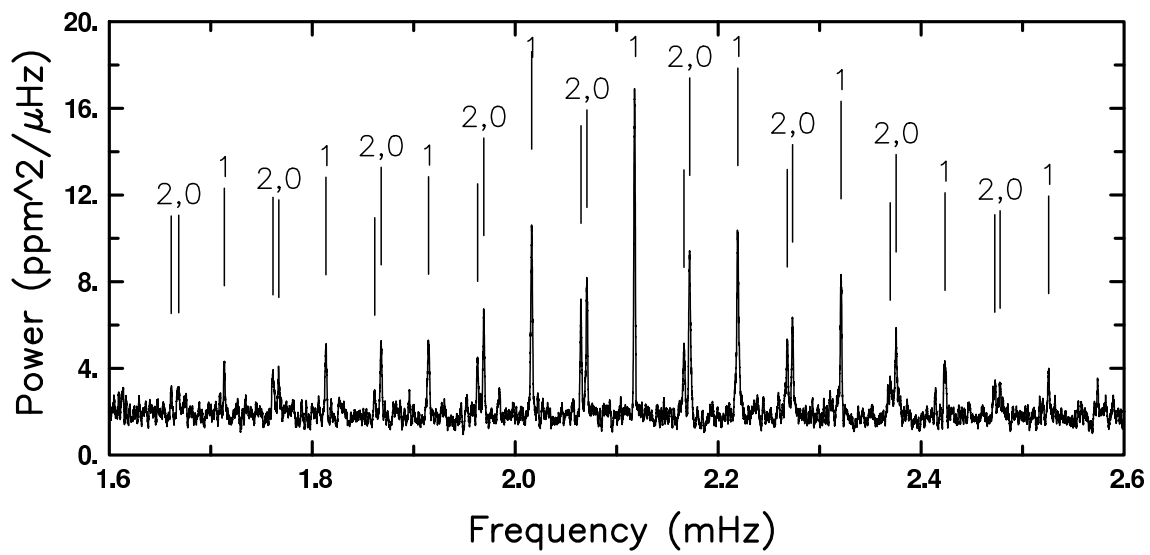
Gilliland *et al.*

FIG. 12.— Power spectrum for Kepler-68 showing strong solar-like p mode oscillations. Numbers above modes indicate the angular degree *l* of each mode used in modeling the stellar parameters.
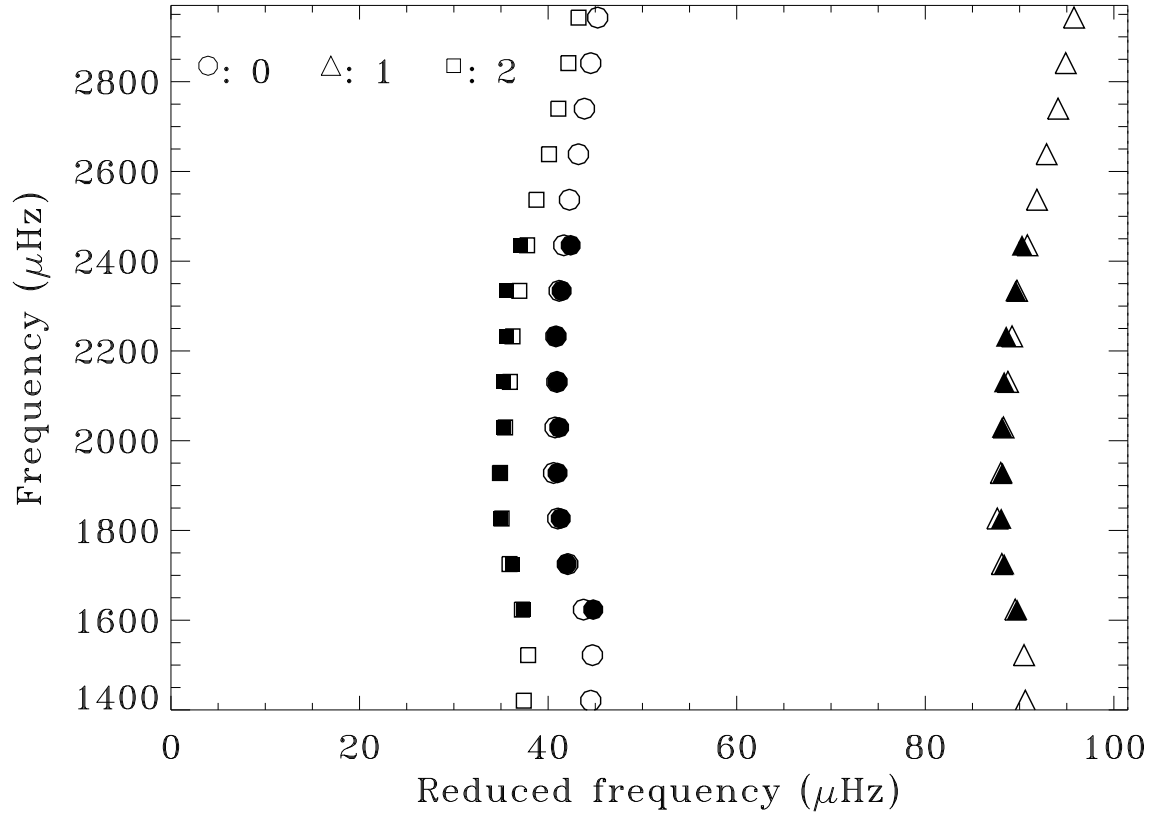
Fig. 13.— Comparison of the observed mode frequencies shown as solid symbols, and those from the best fitting model as discussed in Section 6 shown with the open symbols. The x-axis shows the frequencies after folding by the large separation value of 101.51 μHz. Error bars on the observations are given in Table 3, and are always smaller than the plot symbols.